Assessment of an extended SPARSE model for estimating evapotranspiration from directional thermal infrared data

Samuel Mwangi, Gilles Boulet, Albert Olioso

Assessment of an extended SPARSE model for estimating evapotranspiration from directional thermal infrared data

Samuel Mwangi[1*], Gilles Boulet[1*], Albert Olioso[2]

[1]*CESBIO, Université de Toulouse (CNES/CNRS/IRD/UPS/INRAE) – UMR5126, 18 Av. Edouard Belin, 31401 Toulouse, France*
[2]*EMMAH, INRAE/UAPV – UMR1114, Avignon, France*

[*]*Correspondence to: S. Mwangi (mwangis@cesbio.cnes.fr)*

Abstract

The spatial distribution of evapotranspiration is often obtained from dual source energy balance models forced by surface temperature data. The use of multi-angular remotely-sensed thermal data in such methods makes them susceptible to directional-anisotropy/thermal-radiation directionality effects that may result from the satellite's position, relative to the Sun, at overpass time. It is therefore important to have these effects accounted for to ensure realistic flux retrievals irrespective of sensor viewing position. At present, dual source models generally interpret surface temperature according to two sources, representing the soil surface and the vegetation. This may be insufficient to adequately represent the limiting temperature conditions that not only depend on the source type but also their exposure to the Sun. Here, we present a modified version of the SPARSE (Soil Plant Atmosphere Remote Sensing Evapotranspiration) model, wherein the original SPARSE is modified to incorporate sunlit/shaded soil/vegetation elements and coupled with a radiative transfer model that links these four component emissions to out-of-canopy directional radiances as observed by remote sensors. An initial evaluation is carried out to check the model's capability in retrieving surface fluxes over diverse environments instrumented with in-situ thermo-radiometers. When run with nadir-acquired thermal data, both algorithms show no observable difference in their retrieval of total fluxes. We nonetheless show that by incorporating the solar direction and discriminating between sunlit and shaded elements,

the partitioning of these overall fluxes between the soil and vegetation can be improved especially in water-stressed environments. We also test the sensitivity of flux and component temperature estimates to the viewing direction of the thermal sensor by using two sets of TIR data (nadir and oblique) acquired simultaneously to force the models and show that sensitivity to viewing direction is significantly reduced. This is an important aspect particularly when using high resolution spatial and temporal data from Earth observation missions that inherently have to consider a wide-range of viewing angles in their design.

Keywords: Evapotranspiration, thermal infrared radiation (TIR), Soil Vegetation Atmosphere Transfer (SVAT), temperature inversion.

1. Introduction

Evapotranspiration (ET) plays a key role in mass and energy interactions in the soil-vegetation-atmosphere domain, making its estimation important in applications related to hydrology, agriculture, weather and climate studies. In crop water-use management, accurate ET translates to improved water stress detection, which is important especially in arid and semi-arid regions where ET has been shown to account for more than 90% of the precipitation (Huxman et al., 2005) hence to a large extent controlling the water budget. Transpiration has also been found to account for *ca.* 61% of the global terrestrial ET (Schlesinger & Jasechko, 2014) highlighting the importance of evapotranspiration partitioning. Operationally applicable ET models are therefore of key significance to water resource stakeholders for adequate water-use quantification and its efficient allocation particularly in water-limited areas.

Theoretically, one of the methods used to estimate evapotranspiration involves solving the surface energy budget equation for a surface temperature that results from the aggregation of the

various temperature sources within the soil-canopy system and observed by remote sensors. The energy partitioning can either be: single- (e.g., Surface Energy Balance System (SEBS, Su, 2002)) if one single temperature is used to compute all fluxes; or dual-source if the surface is represented by two bulk temperature sources, one for the soil component considered as a homogeneous isothermal surface and another for the vegetation component seen as a big transpiring leaf, also isothermal (e.g., SPARSE, Boulet et al., 2015 and Two-Source Energy Balance, TSEB, Norman, Kustas, & Humes, 1995). In addition to allowing the partitioning between evaporation and transpiration, the development of dual source models was also meant to realistically address the contribution of varying soil and vegetation skin temperatures to the aerodynamic temperature, which influences the sensible heat flux (Boulet et al., 2012). While remotely-observed radiometric temperature can be defined as the soil and vegetation temperatures weighted by their relative cover fraction in the viewing direction, the link of these component temperatures to the aerodynamic temperature is described according to turbulence resistance between the aerodynamic level and the soil and the vegetation (Norman et al., 1995). Since source temperatures (i.e., sunlit and shaded elements of the soil or vegetation) may exhibit large differences depending on their exposure to the Sun, it is necessary to incorporate the source temperature variations to enable a more accurate representation of conditions at the aerodynamic level.

To drive such surface energy balance models, measurements from in-situ stations have primarily been used as forcing input. The advent of remote sensing (RS), which provides observations of Earth surface characteristics e.g. surface brightness temperature, soil moisture, vegetation indices, albedo etc., has made estimation of land surface fluxes at various spatial and temporal scales more practical. Of the terrestrial state variables retrievable from space, land surface

temperature (LST) is tightly linked to the surface turbulent fluxes and plant water stress hence its ubiquitous use in ET estimation methods. While in-situ thermal infra-red (TIR) sensors can provide point measurements from a fixed direction (generally from nadir or close to nadir), space-borne sensors, which provide observations at larger spatial scales, often view pixels on Earth from varying directions each observation instance. For example, the Moderate Resolution Imaging Spectroradiometer (MODIS) sensor aboard the Terra and Aqua satellites provides, among other products, global LST at a spatial resolution of ~1 km every 1 to 2 days and over a broad-range of viewing angles ($\leq 65°$). The newly proposed Thermal infRared Imaging Satellite for High resolution Natural resource Assessment (TRISHNA) mission, instituted by the French (CNES) and Indian (ISRO) Space Agencies, is also expected to provide global LST products with a revisit time of ~3 days (Lagouarde et al., 2019). Its high spatial resolution (~57m at nadir) and relatively wide field-of-view ($\pm 34°$) should enable multi-scale monitoring of the water and energy budgets. Directional effects can however impact the accuracy of surface state variables inferred from such thermal data.

The need to incorporate directional aspects has necessitated the use of simple radiative methods that link the observed brightness temperature with the prevailing component temperatures, particularly in dual-source models. These, however, do not account for the solar-Earth-viewing geometry, which can lead to significant thermal radiation directionality (TRD) effects (also referred to as TIR directional anisotropy); an extreme case of TRD is the hotspot effect that results from the syzygy Sun-satellite-Earth configuration, where the sensor mostly observes sunlit elements. According to Kimes & Kirchner (1983), Lagouarde et al. (2014) and Duffour et al. (2016), oblique-nadir temperature differences (i.e., thermal radiation directionality) can reach 15 °C. Since LST uncertainties of 1-3 °C may in-turn result in flux errors in the order of ~100

94 Wm^{-2} (Kustas & Norman, 1996), accounting for anisotropy in evapotranspiration models has the
95 potential of significantly improving the derived estimates. Formulations that address thermal
96 radiation directionality, and thus the hotspot phenomenon, are fundamentally extensions of the
97 optical domain's reflectance theory. As detailed in Cao et al.'s (2019) review, they range from
98 geometric, parametric, hybrid to 3-D radiative transfer models.

99 For dual-source evapotranspiration models, it is more suitable to invert component temperatures
100 using radiative transfer or hybrid methods. Bian et al. (2018) recently developed the physically-
101 based unified four-component (UFR97) model. Their radiative scheme is an extension of the
102 two-component Francois et al.'s (1997) model and incorporates bi-directional aspects from Yan
103 et al. (2012). They tested the model on homogeneous, row-crop and forest covers (assuming a
104 spherical foliage projection) where they showed that it could satisfactorily simulate directional
105 temperatures with component sunlit/shaded soil/vegetation temperatures used as input. The
106 relatively easy to implement UFR97 method can thus be used for direct assimilation of
107 directional TIR data and thereby help to address directional anisotropic issues in surface energy
108 balance inversion schemes.

109 In this study, we present an evaluation of a coupled SPARSE-UFR97 model (hereafter
110 SPARSE4) meant for inverting directionally anisotropic thermal data for evapotranspiration and
111 water stress estimation. By coupling SPARSE with the UFR97 radiative method, the original
112 scheme was extended from a two- (soil/vegetation) to a four-component (sunlit/shaded
113 soil/vegetation) formulation. The dual-source SPARSE model, which inverts surface temperature
114 for source emissions and separate retrieval of soil evaporation and vegetation transpiration
115 fluxes, has already been extensively assessed and shown to be capable of reasonably estimating
116 and partitioning turbulent fluxes. In the next section, we introduce the theoretical and

implementation aspects behind the original and extended SPARSE models. The formulations are then evaluated and their performance analyzed using field measurements collected from diverse environments, which include two olive Orchards and two other experimental sites (cultivated with soybean and wheat). Finally, conclusions are drawn and outlooks on continuing and future works with respect to thermal radiation directionality assessments are presented.

2. Materials and Methods

2.1. Theory: SPARSE and SPARSE4 model description

Radiation controls the turbulent fluxes at and near the Earth surface. For energy conservation, the net radiation (R_n) is dissipated in turbulent and conduction heat flux exchanges as:

$$R_n = (1 - \alpha_{sf})S\downarrow + L\downarrow - L\uparrow = H + G + \lambda E \quad (1)$$

where $S\downarrow$ is the incoming shortwave radiation (bottom of atmosphere; BOA); α_{sf} is the surface albedo; $L\downarrow = \varepsilon_a^{cs}\sigma T_a^4$ - incoming long wave radiation emitted by atmospheric constituents (a : clouds, aerosols and gasses); the apparent emissivity ε_a^{cs} is derived according to Brutsaert (1975) in clear-sky situations (which are the relevant situations when using TIR data from satellites); σ is the Stefan Boltzmann constant; and T_a the air temperature. $L\uparrow = \sigma T_B^4 = \varepsilon_{sf}\sigma T_{rad}^4 + (1 - \varepsilon_{sf})L\downarrow$ - outgoing long-wave radiation corresponding to the emission by the surface and the reflected incoming long-wave radiation; ε_{sf} is the surface emissivity and T_{rad} is the surface/radiative temperature; T_B is the brightness temperature as measured by a thermo-radiometer. H denotes the sensible heat flux, G the ground heat flux and λE the latent heat flux. When dealing with remotely sensed thermal data, all used terms are instantaneous (as at the satellite overpass time).

Dual-source energy partitioning in SPARSE consequently involves splitting the single-source

energy balance (Equation (1)) between the vegetation and the soil. The out-of-canopy thermal radiance as observed by a remote sensor is thus treated as a weighted composition of vegetation and soil emissions. To calculate the emissions, and thus the net radiation, component temperatures are required. These soil/vegetation temperatures can then be linked to the remote thermal observation depending on their respective fractions in the viewing direction. In SPARSE4, sunlit and shaded elements of the soil and vegetation sources are discriminated and consequently linked to the measured directional temperature using the Unified Francois model (UFR97, Bian et al., 2018). A synopsis of the similarities and differences between SPARSE and SPARSE4 models is presented next starting with the radiative transfer scheme, the net radiation partitioning, the other energy balance components and finally the implementation framework.

2.1.1. Out-of-canopy radiance

The general form of the link between surface component temperatures and the out-of-canopy radiance in the viewing direction of a remote sensor can be written as;

$$L^{\uparrow}_{rad,\lambda}(\theta_v) = \tau_{\omega}(\theta_v)\varepsilon_{g,\lambda}B(T_g) + \left(1-\tau_{\omega}(\theta_v)\right)\varepsilon_{v,\lambda}B(T_v) + \left(1-\varepsilon_{sf,\lambda}\right)L^{\downarrow}_{\lambda}, \quad (2.a)$$

$$= K_g\tau_{\omega}(\theta_v)\varepsilon_{g,\lambda}B(T_{gs}) + K_z\tau_{\omega}(\theta_v)\varepsilon_{g,\lambda}B(T_{gh}) + \omega_{\omega,s,\lambda}(\theta_v)B(T_{vs}) + \omega_{\omega,h,\lambda}(\theta_v)B(T_{vh}) + \left(1-\varepsilon_{sf,\lambda}\right)L^{\downarrow}_{\lambda}, \quad (2.b)$$

SPARSE applies Equation (2.a) by considering the soil and vegetation sources whereas SPARSE4 uses Equation (2.b) to separate sunlit/shaded elements in the viewing direction. In the UFR97 model (Bian et al., 2018), Equation (2.b) acts as the main link between the separate sunlit/shaded element emissions and the remotely-observed radiative temperature. The terms in the effective emissivities for sunlit/shaded soil/vegetation ($K_g\tau_{\omega}(\theta_v)\varepsilon_{g,\lambda}$, $K_z\tau_{\omega}(\theta_v)\varepsilon_{g,\lambda}$, $\omega_{\omega,s,\lambda}(\theta_v)$ and $\omega_{\omega,h,\lambda}(\theta_v)$, respectively) are given in Appendix A and further detailed in Bian et al. (2018), Francois et al. (1997) and Yan et al. (2012) - K_g and K_z are the sunlit and shaded

fractions of the soil, respectively; τ_ω is the gap fraction; $\varepsilon_{g,\lambda}$ the soil emissivity; $\omega_{\omega,s,\lambda}$ and $\omega_{\omega,h,\lambda}$ are the effective emissivities of sunlit and shaded vegetation. $T_{v,s|h}$ and $T_{g,s|h}$ are the, vegetation and soil component temperatures, respectively; s – sunlit and h - shaded elements. $B(.)$ is the blackbody (Planck's or, as used herein, Stefan Boltzmann) function. Olioso (1995) noted that significant errors could arise if the measuring spectral window of the sensor is not taken into account. Scaling to within the 8-14 μm spectral band (e.g., apogee radiometer specification) is therefore implemented following Olioso (1995) (see Appendix B). Subscript λ holds for the IRT sensor spectral window.

$1 - \tau_\omega(\theta_v) = f(\theta_v)$ is the fraction of radiometer's field of view that is occupied by the canopy, which is a function of view zenith angle $\left(\theta_v = \cos^{-1}(\mu_v)\right)$ and vegetation cover fraction ($f_C = 1 - \tau_\omega = 1 - e^{-G \cdot LAI}$ for a homogeneous cover – applied throughout this study), i.e.:

$$f(\theta_v) = 1 - e^{-G \cdot LAI/\mu_v} \quad (3)$$

LAI here is the effective leaf area index, which is the product of the clumping index and the real LAI of the canopy (Nilson, 1971). It is important to account for the clumping index in non-continuous canopies. For the leaf projection factor, G, a spherical foliage ($G = 0.5$) is assumed with formulations for other leaf inclination distributions defined following Nilson (1971). It should be noted that for the vegetation fraction, the gap fraction (τ_ω) is defined from nadir view (i.e., $\cos^{-1}(\mu_v) = 0°$), Emissivity of the entire canopy ($\varepsilon_{sf,\lambda}$) is given by Francois et al. (1997) as:

$$\varepsilon_{sf,\lambda}(\theta_v) = 1 - \tau_\omega(\theta_v)M\left(1 - \varepsilon_{g,\lambda}\right) - \alpha[1 - \tau_\omega(\theta_v)M]\left(1 - \varepsilon_{v,\lambda}\right) \quad (4)$$

where α is the cavity effect factor (François, 2002; Francois et al., 1997), which defines part of the incident radiation that is reflected by the leaves and finally absorbed by the canopy. Fitting

the α vs θ_v data provided in François (2002) yields $\alpha = 0.3168 + 0.0029\exp(0.0605 \cdot \theta_v)$; an alternative option suitable for large view zenith angles, i.e. a regression based on the α-θ_v data of the canopy-emissivity model (C-EP, Cao et al., 2018), is also included; $M = \frac{1}{\pi}\int_{-\pi/2}^{\pi/2} \tau_\omega(\theta)d\theta$ is the hemispherical gap fraction (Francois et al., 1997). All other terms are as previously defined.

2.1.2. Net radiation and energy balance

Global solar radiation partitioning, apparent atmospheric emissivity and net radiation

The new formulation needs partitioning of the global solar radiation into its direct and diffuse components. The Erbs et al.'s (1982) clearness method summarized in Appendix C is utilized herein to disaggregate the global radiation into diffuse and direct short wave radiation. The gap fraction in the solar direction (θ_i, ϕ_i) is then used to apportion the direct radiation between the sunlit sources. This gap probability is defined in the solar direction $(\theta_i = \cos^{-1}(\mu_i))$ as $\tau_\omega(\theta_i) = e^{-G \cdot LAI/\mu_i}$ for a homogeneous cover.

For the incoming sky radiance, Brutsaert's (1975) analytical method is used, i.e., $RA = \varepsilon_a^{cs}\sigma T_a^4$; where $\varepsilon_a^{cs} = 1.24(e_a/T_a)^{1/7}$ is the apparent emissivity; e_a and T_a are the air vapor pressure and temperature, respectively. This method however only applies to clear skies and it is therefore necessary to have corrections for overcast days. Herein, the Meeus99 scheme detailed in Annear and Wells (2007) is first used to identify clear days. In the method, the clear-sky solar radiation is computed as a function of parameterized ground surface reflectivity, atmospheric albedo, direct and scattered radiation. While Brutsaert's (1975) method is kept for the clear days, it is modified according to Brutsaert (1982) as detailed in Herrero and Polo (2012) for the apparent emissivity in cloudy conditions. The method introduces a parameterized factor (F) that scales the clear-sky emissivity to cloudy conditions, i.e. $\varepsilon_a = F\varepsilon_a^{cs} = (1 + CN^2)\varepsilon_a^{cs}$; C is a cloud dependent

coefficient (herein tuned using incoming longwave measurements) and N, also an atmosphere-dependent coefficient, is parameterized as a function of clearness and relative humidity following Herrero and Polo (2012).

The incoming solar and sky radiations serve as initial inputs for the net radiation terms. The sunlit and shaded contribution functions detailed for the solar domain in Yan et al. (2012) and also applied (with some modifications) in the thermal spectrum by Bian et al. (2018) are used to partition the incoming short- and long-wave radiations between the sunfleck/shaded components. Presently, the turbid canopy radiative method by Taconet et al. (1986), which is in use in the standard SPARSE model, has been extended to incorporate the sunlit/shaded components (Appendix C). The net short-wave (RG_{xx}) and absorbed sky emission (RA_{xx}) terms are separated from the unknown surface thermal emissions ($L^{\uparrow}_{TIRxx} = f(T_{xx})$) for the net radiation terms:

$$R_{n,xx} = RG_{xx} + RA_{xx} + L^{\uparrow}_{TIRxx} \quad (5)$$

$xx = v, g$ and $xx = vs, vh, gs, gh$ for SPARSE and SPARSE4, respectively; "v" and "g" denote the vegetation and the soil/ground, which can either be sunlit ("s") or shaded ("h") in the extended formulation. Like in the original SPARSE, the surface emission terms ($L^{\uparrow}_{TIRxx}$) are defined around air temperature through a Taylor expansion. Further details in Appendix C.

Energy balance scheme

The SPARSE model (Boulet et al., 2015) is based on the two-source TSEB (Norman et al., 1995) rationale. However, unlike in TSEB, where the potential canopy latent flux is estimated through the Priestley-Taylor method, SPARSE utilizes a Penman-Monteith approximation. It is argued that the Priestley-Taylor coefficient (~1.3) may not be reasonable for natural vegetation and regions with strong vapor pressure deficit (Colaizzi et al., 2012). Priestley-Taylor formulations

have been shown to consistently underestimate transpiration partitioning of total ET, especially in semi-arid lands (Agam et al., 2010). SPARSE also employs bounding similar to SEBS (Su, 2002) where theoretical potential and fully stressed flux limits for the soil and vegetation are derived.

The net radiation ($R_{n,xx}$) terms according to Equation (5) are partitioned for retrieval of the soil (G), sensible (H) and latent (λE) heat fluxes. The available energy is thus written as:

$$R_{n,xx} - G = R_{n,xx}(1- \xi) = \lambda E_{xx} + H_{xx} \quad (6)$$

ξ is the fraction of soil/ground net radiation stored in the soil, i.e., $\xi = G/R_{ng}$. Therefore, $\xi = 0$ for the vegetation layers. For diurnal variations of the ground heat storage, the sinusoidal function by Santanello and Friedl (2003) is also included, i.e., $\xi = \xi_{max} \cdot \cos[2\pi(t + 10800)/B]$; t [s] is the time relative to solar noon, B [s] is a deviation minimization factor while 10800 [s] accounts for the three-hour lag between the maximum incoming radiation and maximum fraction (ξ_{max}).

Soil and vegetation component latent fluxes are treated as representative averages for the surface (here gx = g and vx = v for SPARSE; and gx = gs, gh and vx = vs, vh for SPARSE4):

$$\lambda E_g = \sum_{gx} \frac{\rho C_p}{\gamma} \beta_s \frac{e_{sat}(T_{gx}) - e_0}{r_{as}} \quad (7)$$

$$\lambda E_v = \sum_{vx} \frac{\rho C_p}{\gamma} \beta_v \frac{e_{sat}(T_{vx}) - e_0}{r_{vv}} \quad (8)$$

likewise, the component sensible heat fluxes are defined as:

$$H_g = \sum_{gx} \rho C_p \frac{T_{gx} - T_0}{r_{as}} \quad (9)$$

$$H_v = \sum_{vx} \rho C_p \frac{T_{vx} - T_0}{r_{av}} \quad (10)$$

where ρC_p denotes the volumetric heat capacity of air, γ the psychrometric constant, $e_{sat}(T_{xx}) = e_{sat}(T_a) + \Delta(T_{xx} - T_a)$ is the saturated vapour pressure at temperature T_{xx}, Δ the slope of the vapour pressure-temperature curve at T_a, e_0 is the partial vapor pressure at the aerodynamic level; r_{as} is the soil to aerodynamic level resistance and $r_{vv} = r_{av} + r_{sto}$ the minimum total resistance for latent heat exchange between the vegetation and the aerodynamic level; r_{av} is the vegetation-to-aerodynamic level resistance; r_{sto} is the stomatal resistance (defined below). β_s, β_v are the respective evaporation and transpiration efficiencies, defined as the ratio between actual and unstressed latent heat fluxes in actual surface conditions, functionally equivalent to soil and vegetation surface conductances, respectively. For the dependence of aerodynamic resistance to stability correction, the aerodynamic temperature (T_0), component temperatures (T_{xx}), energy fluxes and e_0 are solved and updated iteratively (Richardson number) until convergence. Similar to SPARSE, aerodynamic resistances are expressed according to Shuttleworth and Gurney (1990). Surface components very often alternate between sun and shade and there is therefore no clear distinction between sunlit/shaded elements. For the evaporation/transpiration efficiencies, only the soil and vegetation sources are hence distinguished with similar (evaporation/transpiration) efficiencies applying to both sunlit/shaded sources.

Canopy stomatal conductance

While Chen and Liu (2020) observe that shortcomings resulting from theoretical and practical issues are more serious in big-leaf photosynthesis than in big-leaf evapotranspiration models,

they recommend theoretical consistency in conductance formulation and aggregation. Owing to the inter-dependence between stomatal conductance and assimilation rate in Ball-Berry schemes (e.g., Collatz et al., 1991; Medlyn et al., 2011), and the necessity to have a method that is theoretically consistent with the physics of the original model, we prefer and consequently retain a conductance scheme that considers the product of several relevant environmental factors as used in SPARSE (Boulet et al., 2015; Braud et al., 1995; Noilhan & Planton, 1989; Olioso et al., 1995). We follow the method by Sinclair el al. (1976) who implemented an irradiance-dependent conductance method for sunfleck/shaded leaves, which is more compatible with SPARSE's model structure. Of critical importance is the proper scaling from leaf to canopy stomatal conductance using the respective sunlit/shaded leaf area indices ($\mathrm{LAI_{vx}}$). The stomatal resistance ($\mathrm{r_{sto}}$) to be aggregated for the minimum resistance to latent heat ($\mathrm{r_{vv}} = \mathrm{r_{av}} + \mathrm{r_{sto}}$) as used in Equation (8) is thus written as:

$$\mathrm{r_{sto}} = \frac{\mathrm{r_{stmin}} \prod f}{\mathrm{LAI_{vx}}} \tag{11}$$

where $\mathrm{r_{stmin}}$ is the minimum stomatal resistance; $\prod f = f_{Rg} f_{ea}$ is the product of environmental factors - f_{Rg} is the radiation factor, which measures the influence of photosynthetically active radiation and f_{ea} is the vapor pressure deficit factor, which represents the effects of vapor pressure deficit of the atmosphere on the surface resistance (Braud et al., 1995; Noilhan & Planton, 1989; Olioso et al., 1996).

In SPARSE (and hence SPARSE4), the stomatal conductance ($\mathrm{g_{sto}} = 1/\mathrm{r_{sto}}$) is coupled with the vegetation efficiency (β_v), a term that is related to the plant-water stress, to derive the latent fluxes. The efficiency can be viewed here as a separate conductance term that represents the impact of water stress (related to soil moisture in the root zone) on the vegetation. Coupling the

two conductance terms allows the derivation of flux estimates in potential as well as in prevailing/actual conditions.

2.1.3. Implementation

SPARSE ($xx = v, g$) separately solves the radiative and energy budgets for the soil (g) and vegetation (v) sources. The two continuity equations (Equations (12.b) and (12.c)) and two energy balance equations, together with the link between the component temperatures and the out-of-canopy radiance (Equation (2. a)) are thus solved for the 6 unknowns, i.e., $T_{xx=g,v}$, T_0, e_0, β_v & β_s. For the new version SPARSE4, there are four components ($xx = vs, vh, gs, gh$) since each source - soil (g) or vegetation (v) - is split into a sunlit (s) and a shaded (h) component. This leads to four energy budget and two continuity equations, which together with the out-of-canopy thermal link (Equation (2.b)) are to be solved to retrieve the 8 unknowns: $T_{xx=vs,vh,gs,gh}$, T_0, e_0, β_v & β_s. Therefore, for both SPARSE and SPARSE4, the system of equations is underdetermined and one unknown must be fixed a priori. The energy budget and continuity equations are written as:

$$\begin{cases} R_{n,xx}(1-\xi) - (H_{xx} + \lambda E_{xx}) = 0 & (12.a) \\ \rho C_p \dfrac{T_0 - T_a}{r_a} = H = \sum_{xx} H_{xx} & (12.b) \\ \dfrac{\rho C_p}{\gamma} \dfrac{e_0 - e_a}{r_a} = \lambda E = \sum_{xx} \lambda E_{xx} & (12.c) \end{cases}$$

where r_a is the aerodynamic-to-reference level resistance; and as noted earlier in the section, ξ only applies to the soil and is set to zero for vegetation elements. Other terms are as defined above.

SPARSE can be run in either ‘retrieval’ (‘inverse’) or ‘prescribed’ (‘forward’) modes. Similar to

TSEB, both modes assume the soil surface layer dries first while the vegetation transpires at potential rate ($\beta_v = 1$). In the 'prescribed' mode, the soil evaporation and vegetation transpiration efficiencies are known and the SPARSE4 model uses a 4-by-4 (2-by-2 for SPARSE) energy budget matrix system to solve for the fluxes and temperatures directly. For consistency, the 'prescribed' mode is used herein as it allows a more straightforward separation of the interacting terms and thus get rid of the system's under determination. The transpiration efficiency is therefore prescribed by initially setting it to ($\beta_v = 1$) and the system of equations solved iteratively by decreasing β_s incrementally from ($\beta_s = 1$) till a value that minimizes the difference between the observed and simulated T_{rad}. If a minimum difference is not reached and the soil is dry (β_s, thus evaporation, close to 0), then one assumes that the vegetation is undergoing stress. β_s is then at its minimum (e.g., $\beta_s \approx 0$) and, similarly, β_v is decreased incrementally until the difference between the observed and simulated radiative temperatures is minimal (i.e. simulated $T_{rad} \approx$ observed T_{rad}).

The simultaneous retrieval procedure of the fluxes and temperatures from the energy and radiative set of equations is illustrated by Figure 1 and summarized by Equations (12.a), (12.b) and (12.c). That is: the incoming short- and longwave radiation fluxes are partitioned between the components; a first guess of the aerodynamic temperature then provides a solution for the component emissions (thus temperatures) for onward derivation of the initial component fluxes; the temperature and partial vapor pressure at the aerodynamic level are then iteratively computed for stability convergence (Richardson number – see section 2.1.2). By modulating the evaporation/transpiration efficiencies, i.e. applying a linear decrement of the efficiencies, the procedure can be repeated until the surface temperature boundary condition is met (i.e. simulated ≈ observed surface temperature).

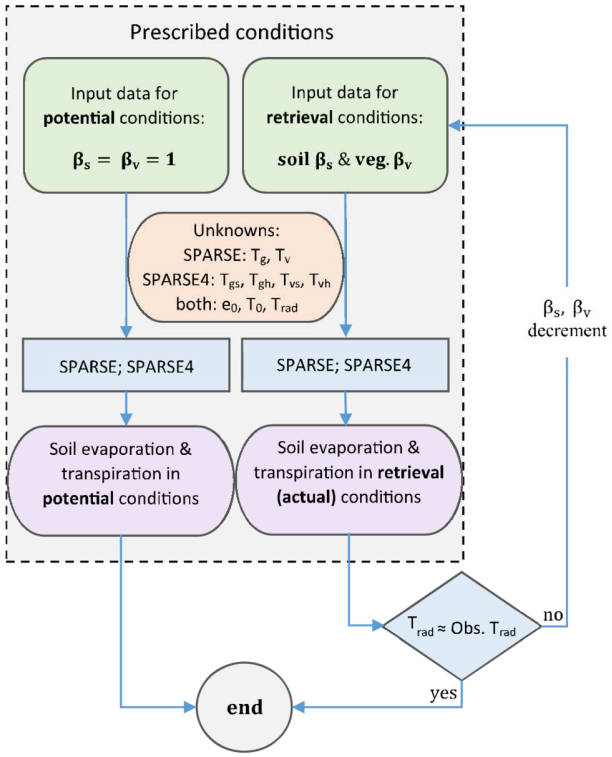

Figure 1: Model flow diagram (adapted from Boulet et al. (2015))

330

331 2.2. Data description

332 2.2.1. Study sites

333 The datasets used to run the models and for performance evaluations are drawn from four
334 contrasting sites. Two Olive Orchards located in: Nasrallah, Tunisia (Latitude, Longitude: 35.30°
335 N, 9.92° E: 2014) and Agdal, Morocco (31.60° N, 7.98° W: 2003) with vegetation cover
336 fractions of ~7% (Chebbi et al., 2018) and ~60% (Er-Raki et al., 2009), respectively.
337 Experimental datasets for the other two sites were collected during the growing periods of
338 Soybean: 1990 (Avignon: 43.90° N, 4.80° E, France; Olioso et al., 1996) and flood-irrigated
339 wheat: 2004 (R3: 31.67° N, 7.59° W, Morocco; Duchemin et al., 2006), hence varying
340 vegetation cover fractions. Table 1 provides a summary of the input data collected from the sites.

These can broadly be categorized into: data used for model runs – meteorological, biophysical information; and evaluation data – flux measurements from the installed radiometers and eddy covariance systems.

2.2.2. Meteorological and surface biophysical input variables

Forcing data collected from the meteorological stations at the four locations include air temperature, relative humidity, wind speed and direction. These are recorded at heights of 9.2, 3, 9.8 and 2 m for Agdal, Avignon, Nasrallah and R3 sites, respectively. Surface temperature, which is needed to force the surface energy balance, is also measured on-site using Apogee Infra-red radiometers (Apogee Instruments Inc., UT, USA) observing from zenith. The R3 study site is also equipped with an oblique-viewing radiometer (at 45° elevation). Surface temperature in Avignon is measured using a Heimann kT17 thermal radiometer. Additionally, incoming solar and sky radiation data from the installed pyranometers and pyrgeometers were available. See Appendix D for a summary of the instruments. Except for Avignon, where recordings were made at hourly intervals, measurements at the other sites were collected on half-hourly basis.

Table 1: Summary of meteorological, biophysical and flux information at the experimental sites (the instruments installed at the experimentation sites are detailed in Appendix D and also presented in the supplementary materials)

Data	Source	Range
Characteristics (both model formulations)		
Surface albedo [-]	*Field: i.e.* $S\uparrow/S\downarrow$	varying
Vegetation albedo; soil and vegetation emissivity [-]	*Literature*	~0.15-0.25; 0.96, 0.98
Bio-physical parameters: leaf area index (LAI – $[m^2m^{-2}]$), leaf inclination distribution function (LIDF - spherical foliage assumed herein: i.e., σ = 0.5 [-]), vegetation height [m], minimum	*Field* Agdal: Avignon: Nasrallah:	LAI; height; $r_{stmin}{}^{*}$ ~1.8; ~6; 200*[a] ~0.4 – 4.0; ~0.2 – 0.8; 80*[b] ~0.21; ~5.8; 200*[a]

stomatal resistance (r_{stmin} - [s m^{-1}]),	R3:	~0 – 4.2; ~0.1 – 0.8; 100*c
Forcing and fluxes (both formulations)		
Meteorological data: Incoming solar radiation (S ↓ - [W m^{-2}]), air & surface temperature [°C], relative humidity [-], wind speed [m s^{-1}]	*Field*	varying
Fluxes [W m^{-2}]: radiation; latent, sensible and ground heat	*Field*	varying
Other data		
Viewing direction: Zenith *(SPARSE and SPARSE4)* and Azimuth *(SPARSE4)*	*Field*	nadir (all sites) and oblique (R3)
Solar direction [°]: Zenith and Azimuth *(SPARSE4)*	*From local time & geo. co-ord.*	as per solar algorithm: ~0 – 90; ~0 – 360

*a Delogu et al. (2018); *b Olioso et al. (1996); *c Boulet et al. (2015), Gentine et al. (2007)

Other than angular data (i.e., viewing azimuth, solar zenith and azimuth angles), no additional information is required to run the extended model for a homogeneous canopy that assumes a randomly inclined foliage. The solar zenith and azimuth angles can be calculated from the local time and geographic coordinates of an area of interest; the Sun angles and daylength algorithm (Campbell & Norman, 1998; Iqbal, 1983) is used herein.

2.2.3. Observations used for evaluation

In all sites but Avignon, sensible and latent energy fluxes were measured using eddy covariance (EC) systems, which consisted of temperature probes, hygrometers, and 3D sonic anemometers that measured the fluctuations of air temperature, water vapor and wind velocity components. The raw EC data at the Agdal site was processed using the 'ECpack' processing tool developed by the Meteorology and Air Quality Group, Wageningen University (Hoedjes et al., 2007). Nasrallah's EC system data was analysed using the 'eddy pro' software developed and maintained by LI-COR Biosciences and the 'ReddyProc' tool used for gap-filling (Chebbi et al.,

2018). For R3, processing of the raw data was done using the 'EdiRe' software package from the University of Edinburgh (Duchemin et al., 2006). The ground heat flux was measured using soil heat plates installed within a few centimeters depth (a correction is applied to account for the heat storage between the sensor and the soil surface). Net radiation was calculated as a residual from the incoming and outgoing short- and long-wave radiation observations from 4 component net radiometers; at Avignon, direct measurements of Rn were performed using 2 component net radiometers. In Avignon sensible heat flux was measured using 1D sonic anemometers and latent heat flux was computed as the residual of the energy balance equation. Latent heat flux was also measured using a Bowen ratio system providing results consistent with the residual method (Cellier & Olioso, 1993). Correction of latent heat fluxes at the R3 wheat field was similarly achieved by ensuring Bowen conservation (Boulet et al., 2015). There was a good daily energy budget closure at the Nasrallah Olive site, which was characterized by a slope of 98 % (Chebbi et al., 2018). An absolute energy closure of 90 % has also been reported for the Agdal Olive site (Er-Raki et al., 2009).

While overall fluxes are important, separating them between the soil and vegetation components is key particularly to users in water deficit regions who are faced with the need to allocate the scarce resource to the plant for optimal agricultural production. Transpiration data were however only available at the Nasrallah and Agdal orchard sites. To allow adequate representation of the olive trees at the Nasrallah site, rescaling of sap-flow observations was necessary. The rescaled measurements were calculated using parameters (i.e., trunk diameter, total stem section) taken from old and young olive trees (Chebbi et al., 2018). For Agdal, data filling was done using a linear regression for the site proposed in Er-Raki et al. (2009), i.e. $0.44\mathrm{ET}_0 + 0.49$; where ET_0 [$\mathrm{mm\ d^{-1}}$] is the daily reference evapotranspiration (estimated in their work using the FAO-

392 56 Penman-Monteith equation).

393 For Nasrallah, performance reporting primarily focuses on the dataset collected over the year
394 2014 whereas some other evaluation variables are drawn from years 2013 and 2015. This is
395 because continuous meteorological, EC and sap-flow data that had minimal errors were readily
396 available for year 2014 while other data were collected in the other years. For instance,
397 measurement of shaded soil temperatures only began in year 2015; however, the turbulent flux as
398 well as sap flow measurements collected during that year had a lot of intermittent but frequent
399 instrument-related errors. In this isolated tree agro-system, positioning an infrared thermometer
400 in the shade or over the sunlit soil was technically straightforward, while the sunlit and shaded
401 leaf elements were more homogeneously distributed and could not fall within the field-of-view
402 (FOV) of a single instrument. We therefore interpreted the difference between a nadir-looking
403 narrow-FOV TIR radiometer and the hemispherical radiometer to retrieve both elementary
404 temperatures. The sunlit vegetation temperature was therefore recomputed from the outgoing
405 longwave radiation (from the hemispherical radiometer), shaded vegetation temperature and
406 sunlit/shaded soil temperatures (from the narrow-FOV TIR radiometers looking at the central
407 canopy gap and bare soil, respectively). That is, the outgoing longwave radiation was assumed to
408 be a function of the bare soil and vegetation (weighted by the gap fraction and foliage cover
409 fraction, respectively) and a small contribution from the reflected sky emittance. From the
410 calculated average foliage temperature, the sunlit vegetation temperature was indirectly solved
411 for by weighting the sunlit/shaded vegetation elements using their respective contribution
412 coefficients from UFR97.

413 ### 2.2.4. Evaporation proxy

414 Save for the hourly-retrieved measurements at the Avignon experimental site, edaphic variables

(i.e., soil moisture and soil temperature) are recorded every 30 minutes. We used the surface soil moisture measurements as a proxy to estimate the evaporation efficiency. Soil evaporation efficiency can be defined as the ratio between actual and potential/maximum evaporation. The 'reference' soil evaporation efficiency (also 'relative humidity at the ground surface' according to Noilhan and Planton (1989)) is given by a sinusoidal function described in Merlin et al. (2011) as:

$$\beta_s = \begin{cases} \left[0.5 - 0.5\cos\left(\pi \frac{\theta_{0-5cm}}{\theta_{max}}\right)\right]^p, & \theta_{0-5cm} < \theta_{max} \\ 1, & \theta_{0-5cm} \geq \theta_{max} \end{cases} \quad (13)$$

where θ_{0-5cm} and θ_{max} are the observed and saturation soil water contents at the surface layer (here volumetric $[m^3m^{-3}]$ soil moisture at 5 cm depth is used); p [-] is a shape parameter related to soil texture. Such a function can also act as an observation operator when assimilating satellite acquisitions of surface soil moisture in soil-vegetation-atmosphere transfer algorithms.

3. Results

3.1. Sunlit and shaded contributions

The Unified Francois (UFR97) model, as detailed earlier, estimates contributions of sunlit and shaded elements depending on the solar and viewing directions. Here we only present a simulated example of the Morocco R3 site as it is the only one with oblique thermal measurements. The site is instrumented with two Apogee Infrared radiometers viewing from nadir and oblique (at 45° inclination). Figure 2 highlights the simulated contributions of the sunlit and shaded soil and vegetation elements. The daily variations are more differentiable in the nadir case where contribution of sunlit elements is highest around solar noon (peaks/troughs in sunlit/shaded element envelopes in Figure 2). With the solar azimuths ranging from 110° - 250°

436 (10 AM - 3 PM), the south-facing off-nadir thermal sensor is simulated to observe varying
437 sunlit/shaded soil elements while mostly viewing the shaded vegetation over the experiment
438 period. This observation is as expected for a site that is located in the Northern Subtropics.

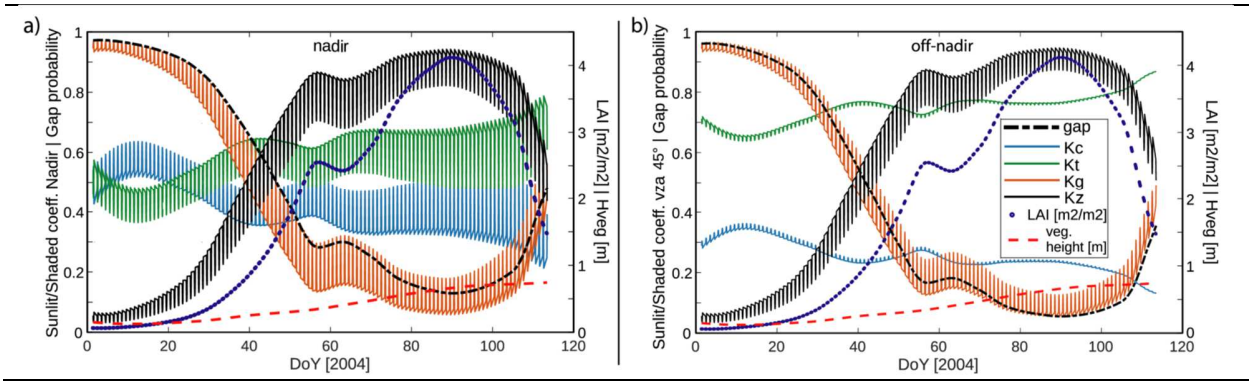

Figure 2: Contributions of sunlit/shaded soil (K_g/K_z) and sunlit/shaded vegetation (K_c/K_t) components and gap fraction (probability) at the R3 wheat site (10 AM - 3 PM) as simulated by the UFR97 method for a) Nadir-, and b) off-nadir/oblique-facing radiometer. Solar noon depicted by peaks in sunlit elements and troughs in shaded elements.

3.2. Global fluxes and partitioning

In this and subsequent sections, the 'prescribed' model runs were forced with surface temperature measurements acquired at nadir, except for the R3 site which also had oblique TIR observations. Performance in estimating total fluxes is analyzed first, then we look at how those fluxes were partitioned between the vegetation and soil sources, and finally on the estimated evaporation efficiency. For an initial overview of how the models perform under different atmospheric conditions, outputs from clear skies were distinguished from cloudy days following the method detailed in section 2.1.2. However, throughout the rest of this study focus is mainly on outcomes from the combined clear-sky and overcast datasets. Further reporting on the nadir- and oblique-derived estimates at the R3 site is discussed in section 4.2. The objective functions used for assessing the performance of the models include: the root mean square error/difference (RMSE [variable's units]), correlation coefficient (R [-]) and bias [variable's units].

3.2.1. Overall (global) fluxes

Daily RMSEs and correlation coefficients for the overall fluxes over the four sites are compared in Table 2 with the columns denoted 'All data' reporting on the combined clear-sky and overcast

458 output. Similarly, Figure 3 illustrates comparisons of the combined data. From inspection of the
459 tabulated metrics, it can observed that even by applying relatively simple sky radiation scaling
460 methods, clear-sky performances can be replicated, i.e., the respective model performances
461 between cloudless and combined outcomes are comparable in all test sites. This highlights the
462 utility of models meant to be used with all-weather remotely sensed data. While this may be
463 desirable temporal-wise, their usage in cloudy conditions would require the use of thermal data
464 that is less influenced by the atmosphere's visibility conditions (e.g. in-situ/field-collected data
465 or unmanned aerial vehicles – UAV imagery), which typically have limited spatial coverage.

466 Some site-specific characteristics could also be observed to influence the overall results. In
467 Nasrallah, for example, the prevailing dry conditions coupled with the fact that only around 7%
468 of the surface is vegetated lead to the flux simulations being mostly attributed to the soil, and
469 more so to the sensible heat flux. With much less available energy being assigned to latent
470 fluxes, relatively low RMSEs could be achieved for the site. However, the latent flux goodness-
471 of-fit for the site as described by the correlation coefficient was not as good although a small
472 improvement could be observed with SPARSE4. Contrarily, at the Agdal orchard - which has a
473 higher vegetation cover fraction and is frequently irrigated - the turbulent fluxes RMSEs are
474 relatively higher but with much better correlation. The hourly performances are displayed in
475 Figure 3 where both models demonstrate nocturnal equivalence with some differences being
476 observed during the day. The relatively large early-morning biases of latent fluxes at the
477 Nasrallah site, which are somewhat reduced in the new model formulation, can also be seen to be
478 averaged out by the reduced nighttime biases.

Table 2: SPARSE and SPARSE4 global fluxes performance: RMSEs [W m^{-2}], correlation coefficients - *R* [-] and bias [W m^{-2}] for the four sites

		SPARSE RMSE/correlation/bias		SPARSE4 RMSE/correlation/bias	
		Clear skies	All data	Clear skies	All data
Agdal	Rn	29/0.99/-19	34/0.99/-24	21/0.99/-4	23/0.99/-5
	LE	64/0.83/11	63/0.82/8	61/0.83/9	57/0.83/6
	H	75/0.87/-29	74/0.86/-28	63/0.88/-12	61/0.88/-11
	G	27/0.88/15	25/0.88/14	27/0.84/2	26/0.84/2
Avignon	Rn	43/0.98/-12	42/0.98/-11	36/0.98/7	38/0.98/7
	LE	44/0.95/-12	43/0.95/-12	48/0.94/2	47/0.94/-1
	H	41/0.90/-13	40/0.89/-14	42/0.78/-4	44/0.77/-3
	G	39/0.89/16	38/0.86/16	39/0.82/11	38/0.80/11
Nasrallah	Rn	35/0.98/-3	34/0.98/4	32/0.98/3	33/0.98/4
	LE	38/0.59/6	39/0.56/7	35/0.62/2	36/0.60/3
	H	48/0.93/-29	47/0.92/-26	44/0.94/-20	44/0.93/-19
	G	42/0.94/13	41/0.93/14	43/0.93/9	41/0.93/12

TIR-view →		***nadir***	***oblique***	***nadir***	***oblique***	***nadir***	***oblique***	***nadir***	***oblique***
R3	Rn	35/0.98/6	36/0.99/7	39/0.98/1	38/0.98/1	41/0.99/13	41/0.99/12	42/0.98/12	43/0.98/11
	LE	48/0.84/-3	46/0.89/5	48/0.83/-6	48/0.87/-1	36/0.94/4	37/0.93/4	40/0.93/5	41/0.91/4
	H	59/0.82/-19	54/0.81/-27	59/0.83/-23	56/0.82/-28	49/0.84/-8	52/0.83/-8	49/0.85/-11	52/0.84/-10
	G	30/0.83/15	32/0.83/16	29/0.82/11	29/0.81/12	37/0.71/6	37/0.70/6	36/0.66/3	36/0.65/3

The net radiation, which is the main source of energy for the system, is observed to be increased with SPARSE4. This tends to reduce the bias (in absolute terms) and the RMSE except in R3. Changes are mostly significant in diurnal periods as shown in Figure 3 and also at night for Nasrallah. In Agdal, the reduced net radiation biases (lower negative biases according to Table 2) also appear to be partly contributed by the relatively higher net radiation for the vegetation (Figure 7). The turbulent fluxes RMSEs at Avignon are fairly higher for the new model. The differences, which can possibly be attributed to the added model complexities, are nonetheless counterbalanced by improved biases. In terms of mean errors, both model formulations appear to consistently overestimate the ground heat flux while generally underestimating the sensible heat fluxes. These biases can mainly be attributed to the estimates at nighttime when the ground

(sensible) heat fluxes are generally overestimated (underestimated). Night soil temperatures estimated by both models generally appear to be underestimated (Figure 5) thus explaining the biases since the low temperatures suggest less soil emissions and therefore more soil net radiation, which is then available for the soil energy fluxes and therefore partly explaining the overestimation of the soil heat flux. The inverse effect of the increased net radiation on sensible heat flux is likely as a result of the inherent/theoretical direct relation between sensible heat flux and temperature and the fact that latent fluxes are capped. The biases are nevertheless somewhat suppressed in SPARSE4 for all fluxes across all sites.

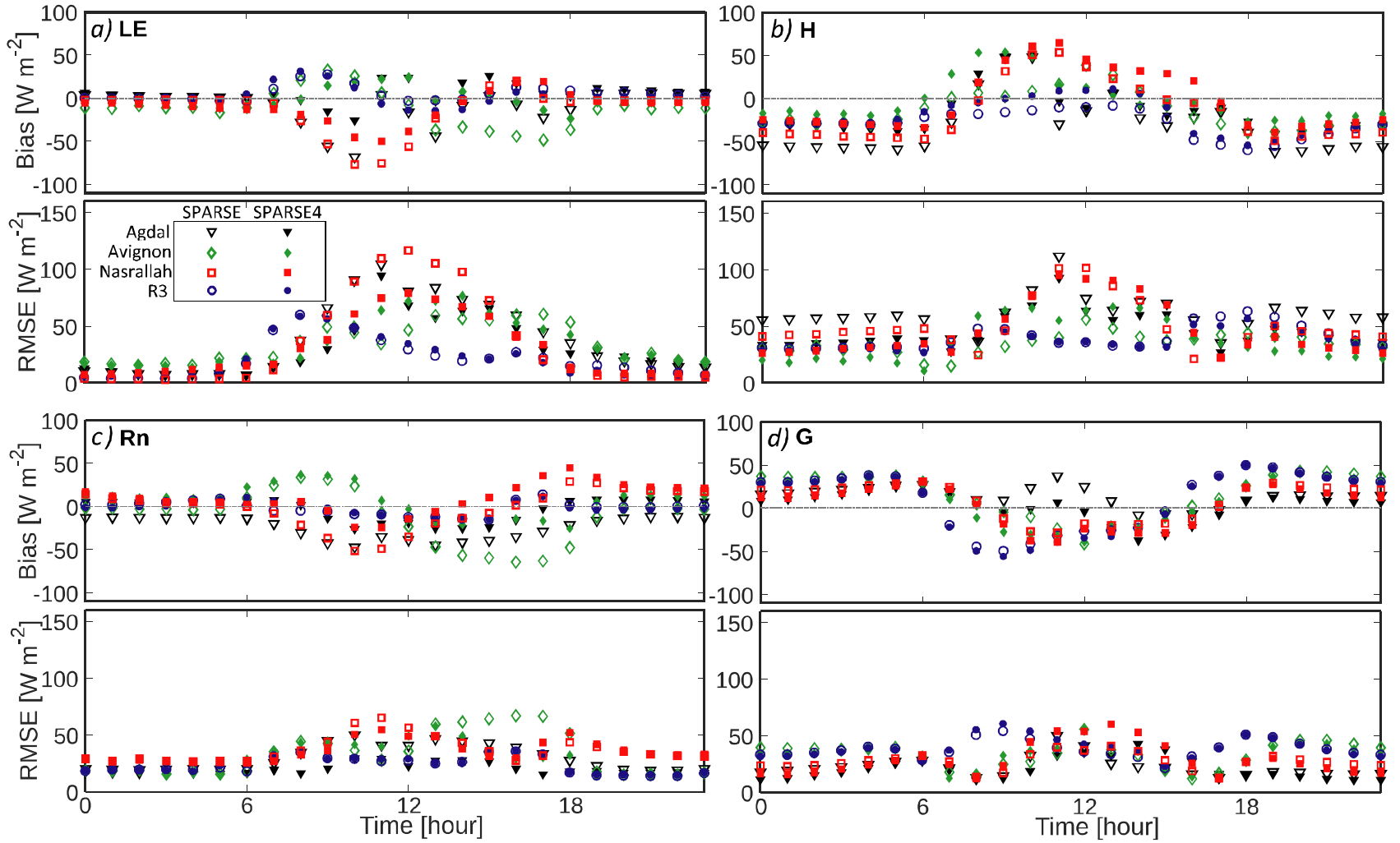

Figure 3: Nocturnal/diurnal trends of bias and RMSEs; for a) latent heat flux, b) sensible heat flux, c) net radiation, and d) ground heat flux. Hollow and solid shapes represent SPARSE and SPARSE4, respectively; shape/color (site): triangle/black (Agdal), lozenge/green (Avignon), square/red (Nasrallah), and circle/blue (R3)

3.2.2. Flux partitioning and temperatures

This sub-section reports on the partitioning of the total fluxes starting with the decomposition of evapotranspiration between the soil and vegetation at the Nasrallah and Agdal orchard sites. As previously noted, availability of sap-flow data is limited to these two sites. The daily transpiration rates simulated during the study periods are illustrated in Figure 4. For Nasrallah, the respective root mean square errors [mm/day], correlation [-] and bias [mm/day] for SPARSE were: $0.15, 0.91, -0.12$; and for SPARSE4: $0.09, 0.90, -0.02$. The models' RMSEs, correlations and bias for Agdal were $0.40, 0.96, -0.35$ and $0.23, 0.96, -0.04$, respectively. The overall reduction of the bias - by at least 40 % - translated to the transpiration in the new formulation being higher than in the standard SPARSE hence allowing the estimates to closely follow the reference observations particularly during the summer.

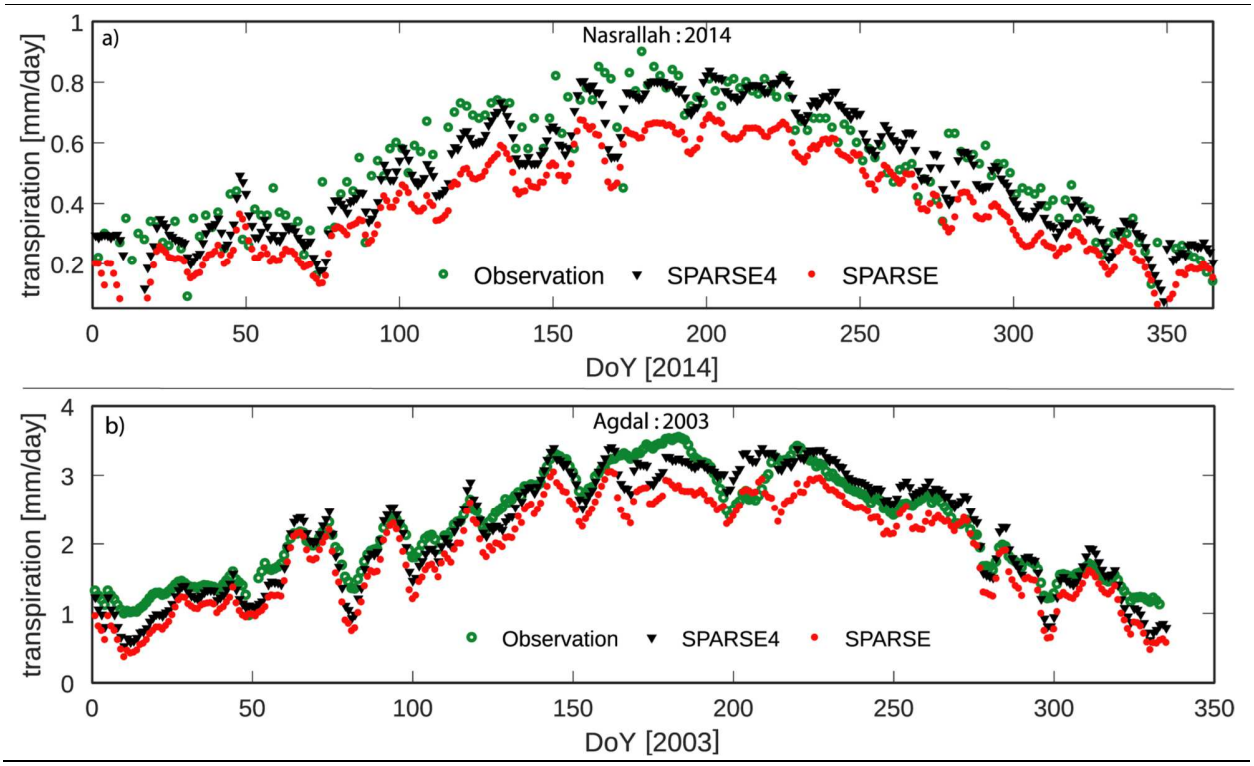

Figure 4: Observed (green o) and simulated (SPARSE: red ●, SPARSE4: black ▼) transpiration –time series' for a) Nasrallah and b) Agdal sites.

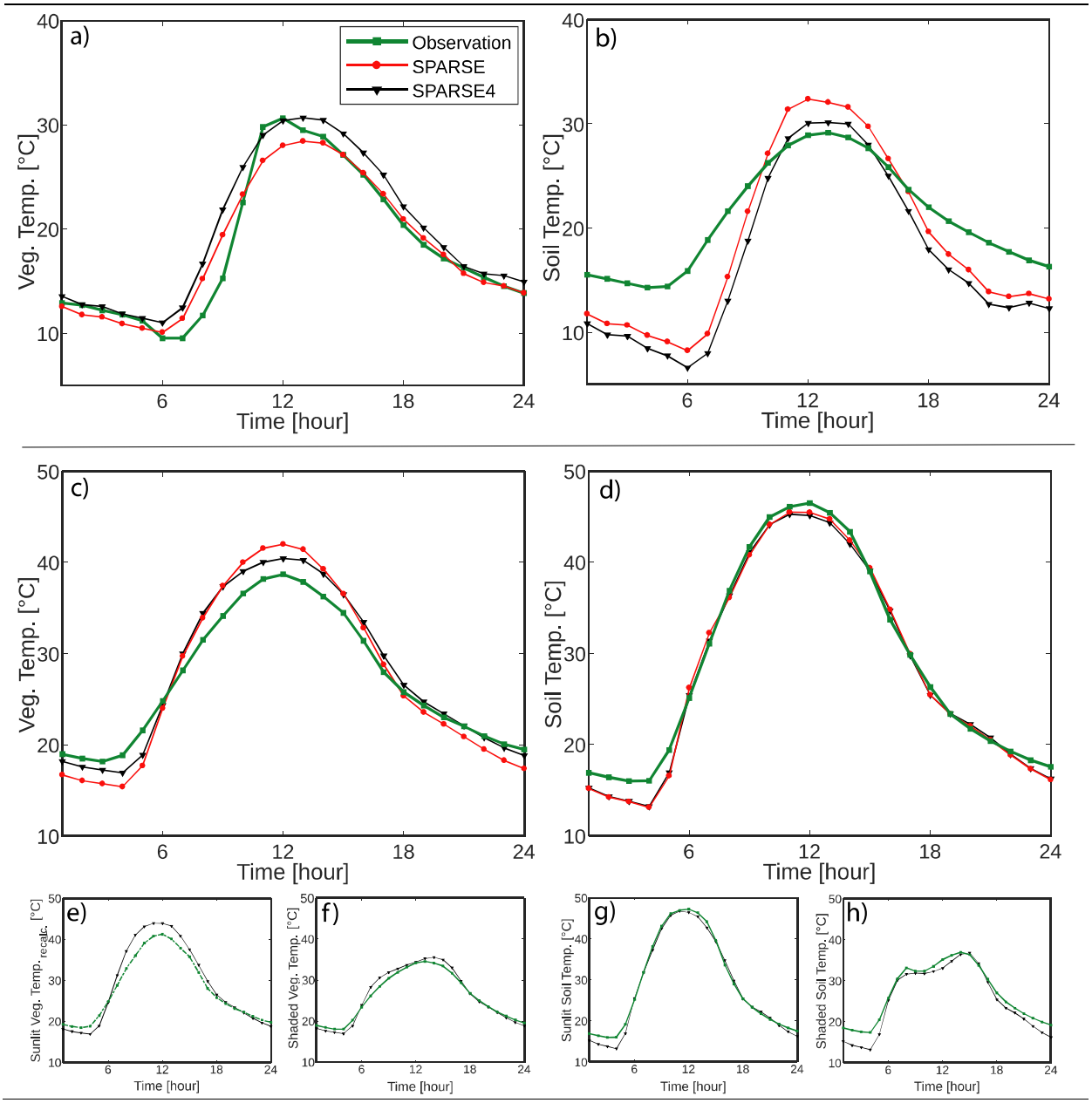

Figure 5: Vegetation and soil temperatures (estimated and observed) over the simulation period in Agdal (a, b) and Nasrallah (c, d); and e, f) sunlit and shaded vegetation elements; g, h) sunlit and shaded soil at the Nasrallah site (key applies to all figures)

508 The simulated temperatures for the Agdal and Nasrallah (2015) sites are shown in Figure 5. For

509 Agdal, the measurements were taken as the soil/vegetation averages. For Nasrallah, however, the

510 sunlit soil, shaded soil and shaded vegetation temperatures were available but only from year

511 2015. As detailed in section 2.2.3, the sunlit vegetation temperature was re-calculated from the

long-wave radiation observations and the measured sunlit/shaded soil and shaded vegetation temperatures. Estimates by SPARSE4, which outputs both shaded and sunlit temperatures, are compared to the observations in Figure 5. The nocturnal soil temperature estimates are generally underestimated resulting in the already noted biases on the soil energy fluxes. The TIR Apogee sensor that provides the shaded soil temperatures (installed under a tree) records slightly higher night temperatures when compared to the sensor in the open field (in the Sun during the day). This phenomenon is however not replicated by the model since the entire soil is considered shaded at night.

3.3. Soil evaporation efficiency

Unavailability of sap flow data due to complexities involved in collecting accurate measurements can make the assessment of evapotranspiration partitioning impractical for some sites. Nonetheless, how well a model estimates vegetation (latent heat) fluxes can be deduced from overall evapotranspiration and soil evaporation. This can practically be obtained as the difference between total evapotranspiration from eddy covariance measurements and soil evaporation inferred from surface soil moisture. Here, we compare the soil efficiencies retrieved by SPARSE to the proxy soil evaporation efficiency given by Equation (13) (Merlin et al., 2011). The modeled soil efficiencies are illustrated and compared to the proxy in Figure 6.

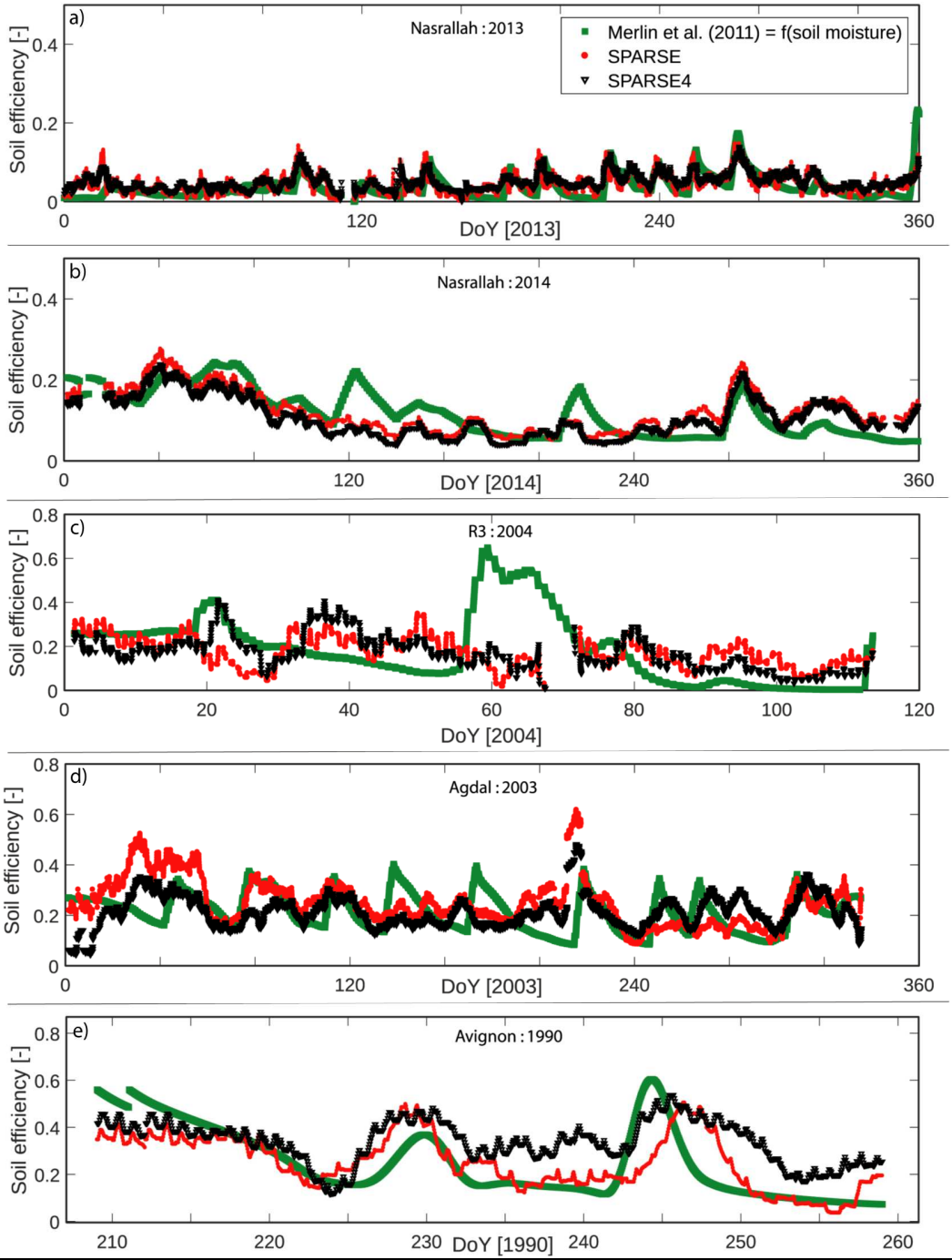

Figure 6: Time series' of soil evaporation efficiencies (SPARSE: red and SPARSE4: black) with Merlin et al.'s (2011) method as the proxy (in green) a, b) Nasrallah - 2013 and 2014, c) R3, d) Agdal, and e) Avignon

529 In Nasrallah, where the soil is greatly stressed, the models' soil efficiency simulations are able to

530 reproduce the 'observation' with both models generally showing a better fit with variations of the

soil moisture inferences. The new scheme appears to capture most peaks in R3 and Agdal, especially around the first soil water inputs, with slightly better timing. Otherwise, the soil efficiency estimations by the two models were almost similar in the four experiments. In addition to the peak in R3 at maximum vegetation development (from DoY ~55 to ~70 excluding missing simulations arising from a surface temperature data gap), some peaks in the evaporation efficiencies at the Agdal site corresponding to irrigation episodes are not well captured.

4. Discussion

4.1. Overall performance and the influence of direction on partitioning

The SPARSE and SPARSE4 energy balance schemes were evaluated over two orchards and two crop experimental sites. Overall, it was apparent that both models could satisfactorily estimate the global fluxes. While there was a general reduction of flux biases with SPARSE4, performance between the models was almost similar when using the nadir-retrieved temperature inputs since such measurements are generally not influenced by TRD effects. These results are expected as all the four sites are situated in relatively high latitudes where directionality effects on the nadir measurements are negligible due to the medium/low Sun angles throughout the simulation periods. R3, which was the only site with an oblique-viewing radiometer, also provided measurements that were simulated to originate from mostly shaded elements as illustrated in Figure 2*.b*. Consequently, the nadir- and oblique-derived total flux estimates were retrieved with reasonable accuracy by both schemes (Table 2). In order to derive differentiated and possibly improved total flux retrievals from the new model formulation, surface temperature differences arising from thermal radiation directionality effects should be present. As reported earlier, directionality effects can be quite large especially when viewing in the solar direction warranting the use of a directionality model to simulate out-of-canopy radiances. These thermal

554 directionality effects could however not be tested at present due to limitations related to
555 unavailability of directional thermal measurements. SPARSE has also been shown to exhibit
556 equifinality (Boulet et al., 2015; Boulet et al., 2018) where consistent/similar total fluxes can be
557 estimated with different stress-level combinations of the individual sources. We acknowledge
558 and expect that this aspect is also present in the new formulation.

559 Figure 7 illustrates the component net radiations as simulated by the two models. Also shown are
560 the vegetation cover fractions in the solar as well as nadir directions. Consideration of the solar
561 direction, i.e. where direct radiation is partitioned with respect to the solar elevation, ensures
562 more radiation is apportioned to the vegetation in the new formulation. The rationale is twofold:
563 1) the diffuse fraction (fd) as defined by Erbs et al. (1982) decreases with increase in the sky
564 clearness index, therefore high global solar radiation will generally result in high direct radiation
565 in the solar direction; and 2) gap fraction – complement to vegetation cover fraction as illustrated
566 in Figure 7 - diminishes (hence canopy fraction increases) from nadir to the Sun's zenith (which
567 is often oblique especially in the subtropics and temperate regions); this additional radiation
568 received by the vegetation can then be partitioned between the turbulent fluxes. Indeed, this leads
569 to the higher vegetation available energy in the Agdal site, which is then apportioned for the
570 higher canopy turbulent fluxes thus the slightly higher transpiration. However, if one assumes
571 minimal errors in the diffuse radiation measurements, then it should be acknowledged that the
572 use of Erbs et al.'s (1982) method introduces additional partitioning uncertainties as depicted by
573 the observed diffuse fraction band in Figure C1. With relatively more radiation reaching the soil,
574 the classical SPARSE model attains a better simulation of the ground heat flux in terms of
575 RMSE and correlation although this appears to in-turn lead to relatively higher positive biases.
576 While the discrimination between shaded and sunlit elements likely results in better partitioning

of vegetation's available energy between sensible (H_v) and latent (LE_v) heat fluxes, the expected impact of vegetation temperatures on the absolute H_v values is not apparent - especially for densely vegetated scenes and unstressed vegetation. When the vegetation is unstressed, the new formulation will generally apportion the relatively higher vegetation available energy as unstressed H_v since LE_{vpot}/Rn_{vpot} is inherently similar to that simulated by SPARSE.

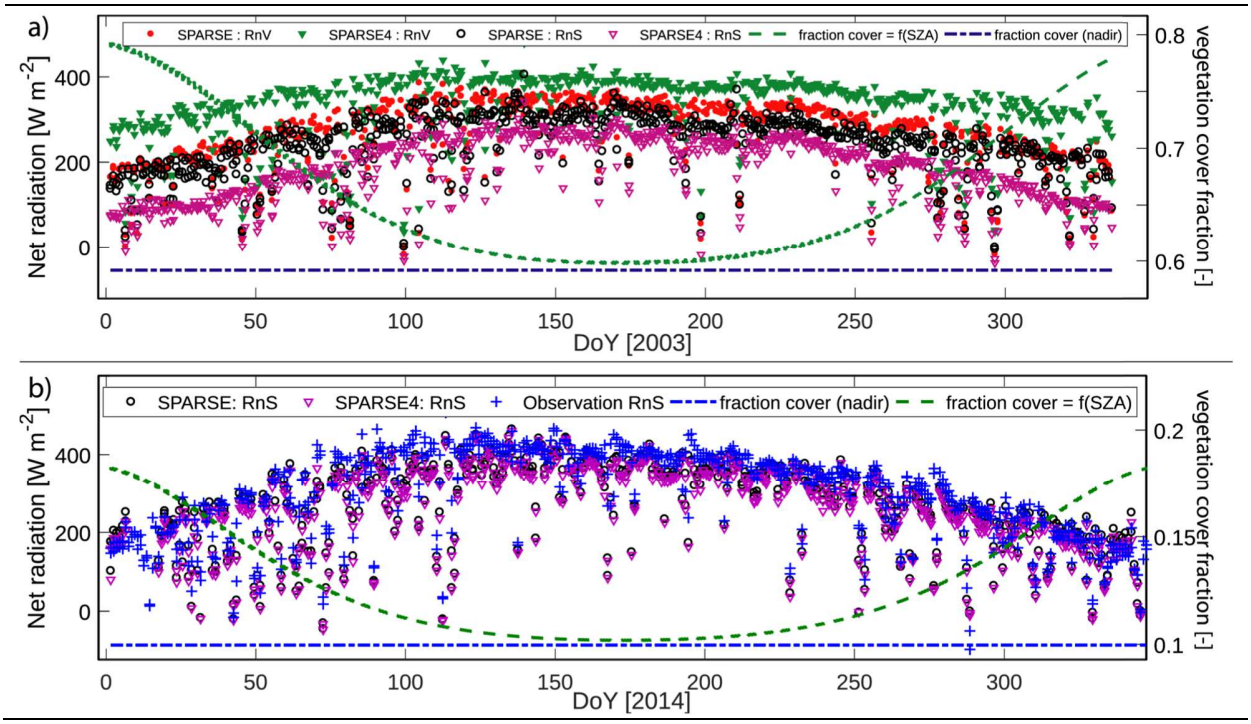

Figure 7: a) Vegetation/soil net radiation (noon) at the Agdal site and b) Nasrallah soil net radiation. Right axis: nadir vegetation cover fraction (only dependent on LAI and LIDF) and vegetation cover fraction in the Sun direction (dependent on LAI, LIDF and solar elevation).

While the UFR97 method provides gap frequencies treatment for homogeneous/continuous covers, row (Yan et al., 2012) and forest (Bian et al., 2018; Li et al., 2017), this study applies the homogeneous method across all sites since it ensured consistency with the observations. When compared to the continuous cover method, Li et al.'s (2017) method has been shown to provide significantly larger gap fractions especially at nadir (Bian et al., 2018). We also observe its underestimation of vegetation cover fraction when compared to the observations at the orchards.

588 The radiative model could nonetheless be improved by using the discontinuous versions, which
589 we expect can further improve the results. The method's suitability in surface energy balance
590 partitioning however requires careful analysis before it can be properly applied. With respect to
591 applying different cavity effect formulations (FR97 and C-EP), we observe that the differences in
592 the resulting fluxes are very small (results not shown). This is because the orders of magnitude of
593 both cavity effect formulations are quite close for nadir views with the differences in the
594 resulting canopy emissivity being marginally higher for larger viewing zeniths.

595 4.2. Sensitivity of estimates to nadir vs off-nadir viewing

596 It is important to test the sensitivity of evapotranspiration derivation methods to the sensor
597 direction of view because prevailing surface condition retrievals (temperatures, radiation and
598 turbulent fluxes) should essentially be similar whatever the geometry of data acquisition. This is
599 a key consideration aspect since space-borne sensors, which presently act as essential sources of
600 input data for Earth observation methods, generally observe terrestrial pixels from off-nadir
601 directions, with the viewing orientations changing often depending on the satellite's location in
602 its orbit. While the Sun-synchronous concept used in some missions (e.g., MISTIGRI,
603 Lagouarde et al., 2013) minimizes the impact of thermal radiation directionality by allowing
604 same viewing geometry for a given location, it cannot entirely eliminate effects resulting from
605 solar position variations (Duffour et al., 2016; Duffour et al., 2015). For instance, future high
606 resolution satellite missions in the TIR domain (e.g., TRISHNA, Lagouarde et al., 2019) will
607 observe a given location with very different observation angles from one overpass to the other.
608 This will allow frequent revisit capacities, which are indeed necessary for reasonable temporal
609 upscaling of evapotranspiration estimates (Delogu et al., 2021). While the retrieval parameters
610 (e.g. overpass time) can be duly chosen such that the hotspot is rarely observed, these

611 specifications mean that it is likely for the sensors to acquire remote sensing data close to the
612 hotspot particularly over the tropics and subtropics (see for example Duffour et al. (2016)).
613 Additionally, directionality is also an issue for current missions including MODIS, and is usually
614 ignored (except for the amount of vegetation in the sensor's field of view). SPARSE 4 was
615 designed to account for such differences in viewing direction and changes in Sun position, and it
616 is important to evaluate potential improvements in this sense comparatively to SPARSE. We
617 therefore test the models' output sensitivity to observation angle for the R3 site when forced with
618 surface temperature observations acquired simultaneously either at nadir or from a 45° (south-
619 facing) elevation angle.

620 Figure 8 plots the oblique- against nadir-retrieved model estimates for the two SPARSE
621 formulations and the performance evaluation of the respective nadir and oblique simulation sets
622 are tabulated in Table 2. The small differences between the temperatures observed from the two
623 directions (within ~3°C) allow the overall fluxes to be satisfactorily reproduced by both models.
624 Reproduced retrievals of vegetation fluxes by SPARSE4 however appear better and it can also be
625 observed that angular surface temperature inputs have slightly more impact on SPARSE's
626 retrieval of soil temperatures. This can in part be explained by the fact that the gap fraction
627 reduces from nadir to off-nadir and the underlying physical assumption of the soil being stressed
628 prior to vegetation. This lower oblique gap means that the fraction of soil (and hence its
629 contribution to the signal) in the field of view of the sensor is reduced leading to variations in the
630 simulated soil stress efficiency and thus the soil temperatures. Additionally, the coupling of the
631 soil and vegetation in the net radiation scheme means any deviations in soil emissions ultimately
632 influence the vegetation's radiative and energy budgets. The influence on soil fluxes in extended
633 model can be interpreted the same way although its consideration of the shaded soil (which

reduces the average temperature variations) appears to diminish the overall effect. There is consequently a tendency to simulate similar, albeit potential *(subscript $_{pot}$)* or unstressed, vegetation fluxes in both SPARSE4 scenarios.

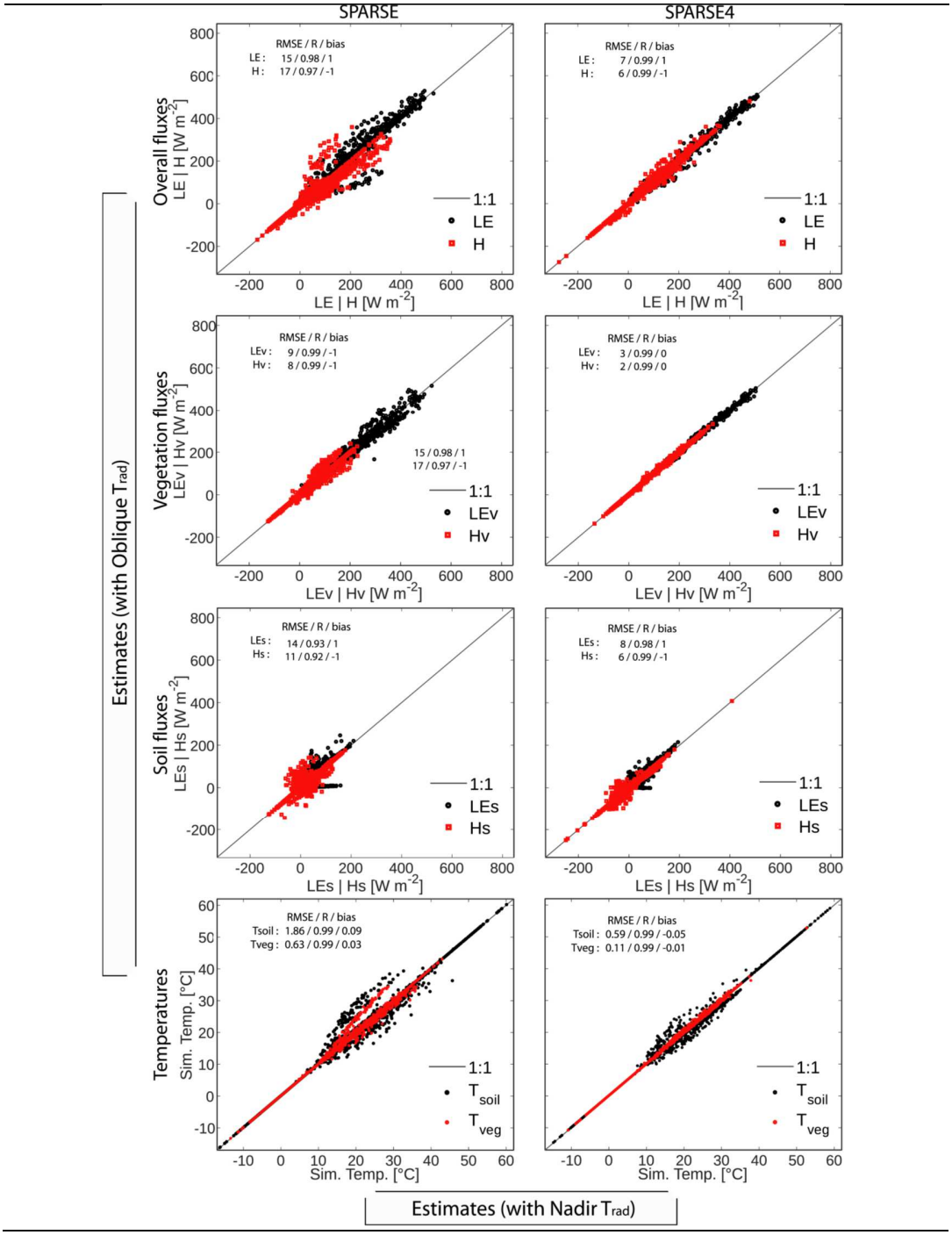

Figure 8: Sensitivity of estimates to angular thermal data. I.e.: estimates using oblique-observed

T_{rad} (ordinate) vs estimates from nadir-observed surface temperature (T_{rad}) input (abscissa). Inset: RMSE, R and bias of oblique-based estimates versus nadir-based estimates.

637 The inversion capabilities of the coupled model are quite promising since it is apparent that, even
638 with thermal data measured from different directions, the prevailing component temperatures and
639 fluxes (radiative and energy) at the land surface can satisfactorily be retrieved and reproduced
640 with SPARSE4 estimates being more consistent when compared to SPARSE's retrievals.
641 Nevertheless, the method's inversion and turbulent flux reproduction capabilities over the entire
642 Sun-observer polar grid requires further verification. Since we also see no observable
643 improvement in overall flux retrievals especially when thermal radiation directionality effects
644 (oblique-nadir temperature differences) are negligible, a study that will encompass a wide-
645 ranging combination of Sun-Earth-sensor geometries (including the hotspot region) is necessary.

646 5. Summary and Conclusions

647 In this study, we have presented an extended formulation of the Soil Plant Atmosphere Remote
648 Sensing Evapotranspiration (SPARSE) model where sunlit and shaded elements have been
649 distinguished in the energy and radiative balance schemes. A clearness index method was hence
650 adopted to partition the incoming global solar radiation into its direct and diffuse components.
651 Since remote thermal infra-red sensors usually observe within a narrow spectral window, a
652 method that accounts for this important aspect has also been incorporated. For thermal radiation
653 directionality effect accounting, coupling was done with the Unified Francois (UFR97) radiative
654 transfer model that links the sunlit/shaded soil/vegetation surface emissions with out-of-canopy
655 radiance in the viewing direction. A preliminary evaluation of the extended method was then
656 carried out to assess its capability in estimating and partitioning overall fluxes on two orchards
657 and over growing cycles of soybean and wheat.

658 We observed that the partitioning of total fluxes does improve when sunlit and shaded elements

659 are distinguished leading to better transpiration estimates especially in water stressed regions. By
660 weighting between shaded/sunlit elements, the tendency by the original SPARSE model to
661 simulate higher vegetation temperatures was also largely reduced. Since remotely sensed data are
662 often acquired from oblique directions, models that invert the measured surface temperatures
663 should be insensitive to any angular effects. It was thus observed that the extended formulation,
664 coupled with an anisotropy model, resulted in better reproduction of flux and component
665 temperature estimates from directional thermal data. This is particularly important when using
666 data whose signal could be influenced by the Sun-Earth-sensor geometry particularly in the
667 hotspot direction. Satellite missions whose objectives include ecosystem functioning and stress
668 monitoring (e.g. TRISHNA, LSTM) can / will be able to provide thermal observations at
669 relatively high spatial and temporal resolutions by proposing a wide range of viewing repeat-
670 cycle angles. While we contend that the new formulation is not meant to replace the standard
671 SPARSE algorithm especially when inverting thermal data less influenced by TRD, its
672 consideration of directionality aspects/effects (which are not only limited to the hotspot region)
673 as well as its demonstrated capabilities of flux partitioning in water-deficit terrains are worth
674 further investigation. These should form part of a future study whose main focus will be thermal
675 radiation directionality effects on turbulent flux estimation. Such analyses should also potentially
676 be able to inform the selection of algorithms that normalize directionality-influenced remote
677 sensing products to a particular standard direction. Introducing clumping index into the modified
678 SPARSE model by considering non-continuous vegetation cover is another valuable work in the
679 future.

680 *Supplementary material and code availability*: supplements are available as a separate file; the
681 code can be accessed through: osr-cesbio.ups-tlse.fr/gitlab_cesbio/mbugu/sparse4

Acknowledgements

This work is supported by the Centre National d'Études Spatiales (CNES) and the Région Occitanie through a fellowship awarded to the first author as well as the CNES funded TRISHNA project. The authors would like to thank the European Commission and ANR for funding in the frame of the collaborative international consortiums FLUXMED and ALTOS financed under the 2018 Joint call of the WaterWorks2017 ERA-NET Cofund and the 2019 PRIMA call respectively. This paper is based on historical data acquired during the scientific activities pertaining to the TREMA (UCA, IRD, ABHT, ORMVAH, DMN, CNESTEN) and NAILA (INAT, INRGREF, IRD) International Joint Laboratories.

The authors thank the Editors and the anonymous referees for their helpful and constructive comments and suggestions.

Appendix A: Contribution of sunlit and shaded elements

The sunlit (K_g) fraction of visible soil is calculated as:

$$K_g = \frac{\exp\left[-\left(\Omega_i \frac{G_i}{\mu_i} + \Omega_v \frac{G_v}{\mu_v} - w\sqrt{\Omega_i\Omega_v \frac{G_i}{\mu_i}\frac{G_v}{\mu_v}}\right) LAI\right]}{b(\theta_v)} \quad (A1)$$

and the complement is the shaded fraction of visible soil:

$$K_z = 1 - K_g \quad (A2)$$

$G_{j=i,v}$ is the foliage projection factor in the viewing (v) or solar/illumination (i) direction; $\mu_{j=i,v}$ is the cosine of an angle; $\Omega_{j=i,v}$ is the clumping index derived by inverting the gap frequency ($b(\theta_v) = \tau_\omega(\theta_v)$) Beer's exponential formula given in Nilson (1971); LAI is the leaf area index; $w = \frac{d}{h\delta}(1 - e^{-h\delta/d})$ is the hotspot function; d and h are the leaf width and canopy height, respectively; $\delta = \sqrt{\tan^2(\theta_i) + \tan^2(\theta_v) - 2\tan(\theta_i)\tan(\theta_v)\cos(\varphi)}$; φ – relative azimuth angle between

703 the solar and viewing directions.

704 Effective emissivity expressions of the sunlit ($\omega_{\omega,s}(\theta_v)$) and shaded ($\omega_{\omega,h}(\theta_v)$) leaves are:

705 $$\omega_{\omega,s}(\theta_v) = [1 - b(\theta_v)]\varepsilon_v K_c + (1 - M)b(\theta_v)(1 - \varepsilon_g)\varepsilon_l C_c + (1 - \alpha)[1 - b(\theta_v)M][1 - b(\theta_v)](1 - \varepsilon_v)\varepsilon_v C_c \quad (A3)$$

706 $$\omega_{\omega,h}(\theta_v) = [1 - b(\theta_v)]\varepsilon_v K_t + (1 - M)b(\theta_v)(1 - \varepsilon_g)\varepsilon_v C_t + (1 - \alpha)[1 - b(\theta_v)M][1 - b(\theta_v)](1 - \varepsilon_v)\varepsilon_v C_t \quad (A4)$$

707 where ε_v and ε_g are the leaf and soil emissivities respectively; α is the cavity effect factor
708 (François, 2002; Francois et al., 1997) that defines part of the incident radiation that is reflected
709 by the leaves and finally absorbed by the canopy. C_c and C_t respectively are the contribution of
710 sunlit and shaded leaves inside the canopy to the radiation emitted from leaves and reflected by
711 the soil. The same factors apply for radiance emitted from the leaves and reflected by other
712 leaves (Bian et al., 2018; Francois et al., 1997). M is the hemispherical average gap frequency
713 (Francois et al., 1997). The respective contributions of sunlit and shaded leaves are (Yan et al.,
714 2012):

715 $$K_c = \frac{\left[1 - \exp\left(-w\sqrt{\Omega_i\Omega_v \frac{G_i}{\mu_i}\frac{G_v}{\mu_v}}\,LAI\right)\right]}{[1 - b(\theta_v)]} \quad (A5)$$

716 $$K_t = 1 - K_c \quad (A6)$$

717 For definition of some terms that were modified when formulating the UFR97 model (e.g.
718 upper/lower layer height and leaf area terms for K_c and K_t) see Bian et al.'s (2018) work.

719 Appendix B: Long-wave radiation in the narrow $8 - 14$ μm spectral band of
720 the observing thermal sensor

721 Field thermo-radiometers usually provide measurement in the $8 - 14$ μm spectral range (it is
722 also common to have satellite radiometers observing in the $10.5 - 12.5$ μm band). The measured
723 thermal radiation is given by (Olioso, 1995):

724 $$f_\lambda(T_B)\sigma T_B^4 = \varepsilon_{surf,\lambda} f_\lambda(T_{rad})\sigma T_{rad}^4 + (1 - \varepsilon_{surf,\lambda})L_\lambda^\downarrow \quad (B1)$$

where σ is the Stefan Boltzmann constant, T_B is the measured brightness temperature, T_{rad} the radiative surface temperature and $L_\lambda^\downarrow$ is the down-welling atmospheric radiation in the narrow observation band. By assuming $f_\lambda(T_B) \approx f_\lambda(T_{rad})$, the unknown T_{rad} can be solved for. $f_\lambda(T)$ and $L_\lambda^\downarrow$ for $\lambda = 8 - 14$ µm are expressed as:

$$f_{\lambda:8-14}(T) = -0.6732 + 0.6240 \cdot 10^{-2} T - 0.9140 \cdot 10^{-5} T^2 \quad \text{(B2)}$$

$$L_{\lambda:8-14}^\downarrow = \varepsilon_{a,\lambda} f_\lambda(T_a) \sigma T_a^4 \quad \text{(B3)}$$

T_a is the air temperature. Likewise, the atmospheric apparent emissivity $\varepsilon_{a,\lambda}$ in the $8 - 14$ µm window is given by:

$$\varepsilon_{a,\lambda:8-14} = 0.15 + 5.03 \cdot 10^{-6} e_a \exp(2450/T_a) \quad \text{(B4)}$$

All temperatures are in [K] and the atmospheric vapor pressure e_a in [hPa]. Further details including formulations for the $10.5 - 12.5$ µm thermal band can be found in Idso (1981) and Olioso (1995).

Appendix C: Global solar radiation partitioning and radiative balance terms

Global solar radiation partitioning

Fraction of incoming diffuse radiation (fd) is estimated following the sky clearness index (K_T) method proposed in Erbs et al. (1982). Where the atmosphere's optical depth data is available, a modified function according to Carrer et al. (2013) is applied for $K_T > 0.80$:

$$fd = \begin{cases} 1 - 0.09 K_T, & \leq 0.22 \\ 0.9511 - 0.1604 K_T + 4.388 K_T^2 - 16.638 K_T^3 + 12.336 K_T^4, & 0.22 < K_T \leq 0.80 \\ 0.165 \mid (1 - \exp(-\tau_{opt}))/(1 - (1 - \mu_s)\exp(-\tau_{opt})), & K_T > 0.80 \end{cases} \quad \text{(C1)}$$

where $K_T = RG/(C_s \mu_s)$ is the clearness index, $RG = S\downarrow$ is the global solar irradiance at BOA, $C_s = 1368\ W\ m^{-2}$ the terrestrial solar radiation constant, μ_s is the cosine of the solar zenith

angle), and τ_{opt} is the aerosol optical thickness. Consequently, $RG = RG_{dir} + RG_{diff} = RG_{dir} + fd \cdot RG$.

Figure C1 illustrates the estimated compared to observed fraction of diffuse (fd) radiation. The sample data used for the diagram was collected at the Bensalem site in Tunisia. The global incoming radiation was measured using a pyranometer with a hemispherical view while the direct radiation was observed using a narrow-view pyrheliometer.

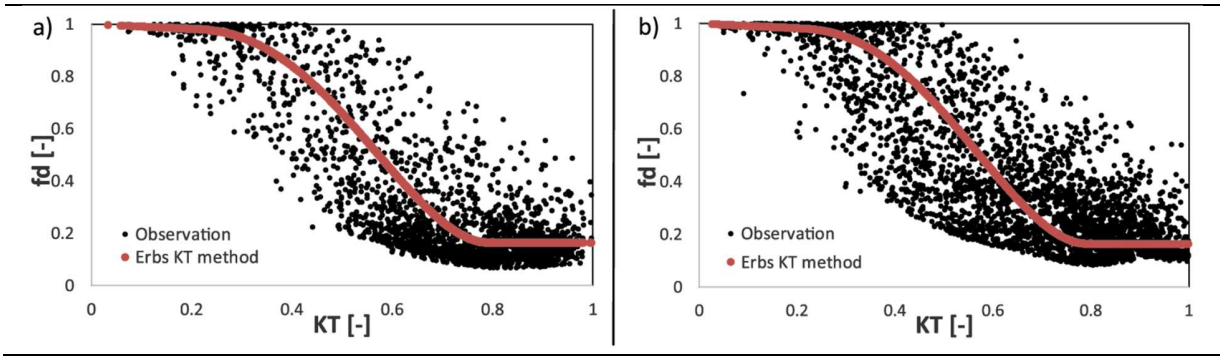

Figure C1: fd (fraction of incoming diffuse radiation) plots using Erbs et al.'s (1982) clearness index (K_T) method on BenSalem dataset for years a) 2014 and b) 2016

Net radiation terms

The incoming solar and sky emission terms are partitioned as:

$$RG_{vs} + RA_{vs} = RG_{dir}\left[f_{sol}(1-\alpha_v) + \frac{f_{vs}\alpha_g(1-f_{sol})[(1-\alpha_v)+\alpha_v f_{vh}]}{1-f\alpha_v\alpha_g}\right] + f_{vs}RG_{diff}\left[(1-\alpha_v) + \frac{(1-\alpha_v)\left[\alpha_v f_{vh}(1-f_{vs}) + \alpha_g(1-f)\right] + \alpha_v f_{vh}\alpha_g(1-f)}{1-f\alpha_v\alpha_g}\right] + f_{vs}RA\left[\varepsilon_v + \frac{\varepsilon_v\left[\rho_v f_{vh}(1-f_{vs}) + \rho_g(1-f)\right] + \rho_v f_{vh}\rho_g(1-f)}{1-f\rho_v\rho_g}\right] \quad (C2.1)$$

$$RG_{vh} + RA_{vh} = RG_{dir}\left[\frac{f_{vh}\alpha_g(1-f_{sol})(1-\alpha_v)}{1-f\alpha_v\alpha_g}\right] + f_{vh}RG_{diff}\left[\frac{(1-\alpha_v)\left[1+\alpha_g(1-f)\right]+\alpha_v f_{vs}}{1-f\alpha_v\alpha_g}\right] + f_{vh}RA\left[\frac{\varepsilon_v\left[1+\rho_g(1-f)\right]+\rho_v f_{vs}}{1-f\rho_v\rho_g}\right] \quad (C2.2)$$

$$RG_{gs} + RA_{gs} = \frac{(1-\alpha_g)\left\{(1-f_{sol})\left[RG_{dir}\left(1+\alpha_v f_{vh}\alpha_g(1-f_{sol})\right)+\alpha_v f_{vh}\alpha_g(1-f)RG_{diff}\right]+f_{gs}RG_{diff}\right\}}{1-f\alpha_v\alpha_g} + \frac{\varepsilon_g RA\left[f_{gs}+(1-f_{sol})\rho_v f_{vh}\rho_g(1-f)\right]}{1-f\rho_v\rho_g} \quad (C2.3)$$

$$RG_{gh} + RA_{gh} = \frac{(1-\alpha_g)\{f_{gh}RG_{diff} + f_{sol}\alpha_v f_{vh}\alpha_g[(1-f_{sol})RG_{dir} + (1-f)RG_{diff}]\}}{1-f\alpha_v\alpha_g} + \frac{\varepsilon_g RA[f_{gh} + f_{sol}\rho_v f_{vh}\rho_g(1-f)]}{1-f\rho_v\rho_g}$$

The grey-body thermal emission is defined around air temperature and estimated through a Taylor expansion:

$$\sigma T^4_{x=vs,vh,gs,gh} = \sigma(T_a + T_x - T_a)^4 \approx \boldsymbol{\sigma T_a^4} + \rho C_p \frac{\mathbf{4\sigma T_a^3}}{\rho C_p}(T_x - T_a) \approx \mathbf{X_{\varepsilon 1}} + \rho C_p \frac{\mathbf{X_{\varepsilon 2}}}{\rho C_p}(T_x - T_a) \quad \text{(C2.4)}$$

Component emissions are:

$$L^{\uparrow}_{TIRvs} \approx \frac{f_{vs}[(\varepsilon_v + \rho_v f_{vh})(\rho_g(1-f_{vh})f_{vs}\varepsilon_v + \varepsilon_g) + \varepsilon_v(\rho_v f_{vh} f_{vs}\varepsilon_v + f_{vh}\varepsilon_v - 2)]}{1-f\rho_v\rho_g} X_{\varepsilon 1} + \frac{X_{\varepsilon 2} f_{vs}}{(1-f\rho_v\rho_g)}\{\varepsilon_v[(\varepsilon_v + \rho_v f_{vh})\rho_g(1-f_{vh})f_{vs} + \rho_v f_{vh} f_{vs}\varepsilon_v - 2](T_{vs} - T_a) + f_{vh}\varepsilon_v^2(T_{vh} - T_a) + (\varepsilon_v + \rho_v f_{vh})[(1-f_{sol})\varepsilon_g(T_{gs} - T_a) + f_{sol}\varepsilon_g(T_{gh} - T_a)]\} \quad \text{(C2.5)}$$

$$L^{\uparrow}_{TIRvh} \approx \frac{f_{vh}\varepsilon_v\left[\left((\rho_v f_{vs} + \rho_g)f_{vh} + f_{vs}\right)\varepsilon_v + \varepsilon_g - 2\right]}{1-f\rho_v\rho_g} X_{\varepsilon 1} + \frac{X_{\varepsilon 2} f_{vh}\varepsilon_v}{(1-f\rho_v\rho_g)}\{f_{vs}\varepsilon_v(T_{vs} - T_a) + [(\rho_v f_{vs} + \rho_g)f_{vh}\varepsilon_v - 2](T_{vh} - T_a) + (1-f_{sol})\varepsilon_g(T_{gs} - T_a) + f_{sol}\varepsilon_g(T_{gh} - T_a)\} \quad \text{(C2.6)}$$

$$L^{\uparrow}_{TIRgs} \approx \frac{(1-f_{sol})\varepsilon_g[(f - f_{vh}f_{vs})\varepsilon_v + \rho_v f_{vh}\varepsilon_g - 1]}{1-f\rho_v\rho_g} X_{\varepsilon 1} + \frac{X_{\varepsilon 2}(1-f_{sol})\varepsilon_g}{(1-f\rho_v\rho_g)}\{(1-f_{vh})f_{vs}\varepsilon_v(T_{vs} - T_a) + f_{vh}\varepsilon_v(T_{vh} - T_a) + [(1-f_{sol})\rho_v f_{vh}\varepsilon_g - 1](T_{gs} - T_a) + \rho_v f_{vh} f_{sol}\varepsilon_g(T_{gh} - T_a)\} \quad \text{(C2.7)}$$

$$L^{\uparrow}_{TIRgh} \approx \frac{f_{sol}\varepsilon_g[(f - f_{vh}f_{vs})\varepsilon_v + \rho_v f_{vh}\varepsilon_g - 1]}{1-f\rho_v\rho_g} X_{\varepsilon 1} + \frac{X_{\varepsilon 2} f_{sol}\varepsilon_g}{(1-f\rho_v\rho_g)}\{(1-f_{vh})f_{vs}\varepsilon_v(T_{vs} - T_a) + f_{vh}\varepsilon_v(T_{vh} - T_a) + \rho_v f_{vh}(1-f_{sol})\varepsilon_g(T_{gs} - T_a) + (f_{sol}\rho_v f_{vh}\varepsilon_g - 1)(T_{gh} - T_a)\} \quad \text{(C2.8)}$$

where $f = f_{vs} + f_{vh}$ (cover fraction) and $1 - f = f_{gs} + f_{gh}$ (gap fraction equivalent to the transmissivity to the background soil) are defined at nadir ($\cos(vza) = \cos(0^0) = 1$); $f_{sol} = f(\theta_s) = 1 - e^{-G \cdot LAI/\mu_s}$. $f_{vs} = K_c f$; $f_{vh} = K_t f$; $f_{gs} = K_g(1-f)$ and $f_{gh} = K_z(1-f)$. K_c, K_t, K_g and K_z are sunlit/shaded contribution terms as previously defined. α_v and α_g are the

783 vegetation and soil albedos (reflectance in the optical domain) while $\rho_v = 1 - \varepsilon_v$ and $\rho_g = 1 - \varepsilon_g$

784 are the thermal reflectance for the vegetation and soil, respectively.

Appendix D: List of instruments

Table 3: Instrumentation (including manufacturer and model) at the experimentation sites

Instrument; Manufacturer; Model	**Agdal** *(Hoedjes et al., 2007; Williams et al., 2004)*	**Avignon** *(Cellier & Olioso, 1993; Olioso et al., 1996)*	**Nasrallah** *(Chebbi et al., 2018)*	**R3** (Boulet et al., 2015; Duchemin et al., 2006)
Radiation	Net radiometer; Kipp & Zonen; CNR1	Net rad. differential pyrradiometer; Crouzet, FR Rg; Kipp & Zonen; CM5	Net radiometer; Husekflux, Delft, NL; NR01 :- SR01, IR01	Net radiometer; Kipp & Zonen; CNR1
Turbulent fluxes	Eddy Covariance (EC) system; Campbell Sci. Ltd., USA; 3D sonic anemometer CSAT3; Hygrometers - CS7500, KH20	1D sonic anemometer - *H*; Campbell Sci., UK; CA27. Residual and Bowen ratio methods – *LE (home built based on a HMP35A Vaisala (Helsinki, Finland) humidity sensor, a differential air pumping system and type T thermocouples; cf.* Cellier and Olioso (1993)	EC system; Campbell, USA; 3D sonic anemometer CSAT3; Hygrometers - LI-COR7200, LI-COR7500	EC system; Campbell, USA; CSAT sonic anemometers; Krypton fast-response hygrometers
Wind speed	Wind vane/anemometer; R.M. Young Co.; WP200	CIMEL (Paris, France) cup anemometer	Anemometer; R.M. Young, USA	Anemometer; R.M. Young, USA; A100R
Relative humidity	Humidity probe; Vaisala, FI; HMP45C	Humidity probe; *HMP35A Vaisala (Helsinki, Finland)*	Humidity probe; Vaisala; HMP155/45	Humidity probe; Vaisala; HMP45C
Air temperature	Temperature probe; Vaisala, FI; HMP45C	Homemade temperature copper probe	Temperature probe; Vaisala; HMP155/45	Temperature probe; Vaisala; HMP45C
Ground heat flux	Heat flux plates; Hukseflux, Delft, NL;	Calorimetric method: i.e., from temperature profiles (type T thermocouples) down to 1 m and soil heat capacity calculated from soil moisture and soil density profiles	Heat flux plates; Hukseflux, Delft, NL; HFP01	Heat flux plates; REBS Inc., USA; HFP3
Surface temperature	Thermo-radiometer; Apogee Inc., UT, USA IRTS-Ps	Heiman kT17 thermo-radiometer, Wiesbaden, Germany	Thermo-radiometer; Apogee Inc., UT, USA IR120	Thermo-radiometers; Apogee Inc.; IRTP1541, IRTP1383

Appendix E: Notations

α	Cavity effect factor [-]
α_g, α_v	Soil/ground (g) and vegetation (v) albedos [-]

β_s, β_v	Soil evaporation and vegetation transpiration efficiencies [-]
Δ	Slope of the vapor pressure-temperature curve at T_a [Pa K^{-1}]
$\varepsilon_a = F\varepsilon_a^{cs}$	Apparent emissivity of the atmosphere [-]. F – parameterization factor for conditions other than cs: clear-sky [-]
$\varepsilon_g, \varepsilon_v, \varepsilon_{sf}$	Emissivity of the soil, vegetation and entire surface, respectively [-]
$\varepsilon_{TIRxx=vs,vh,gs,gh}$	Emitted radiation forcing terms in the net radiation scheme; for sunlit (s) and shaded (h) soil (g) and vegetation (v) [W m^{-2}]
γ	Psychrometric constant [Pa K^{-1}]
$\omega_{\omega,s}(\theta_v), \omega_{\omega,h}(\theta_v)$	Effective emissivity of sunlit and shaded leaves, respectively [-]
$\phi_{j=i,v}$	Solar (i) and viewing (v) azimuth angles [°]
φ	Relative azimuth angle between solar and viewing directions [°]
ρC_p	Product of air density [kg m^{-3}] and the specific heat of air at constant pressure [J kg^{-1} K^{-1}]
σ	Stefan Boltzmann constant [W m^{-2} K^{-4}]
$\tau_\omega \mid b(\theta_v)$	The upward directional canopy transmittance / gap frequency/fraction in viewing direction [-]
$\theta_{j=i,v};\ \mu_j$	Solar (i) and viewing (v) zenith angles; cosine of an angle j [°]
ξ	Fraction of soil/ground net radiation stored in the soil, i.e., $\xi = G/R_{ng}$ [-]
C_c, C_t	Contribution of sunlit and shaded leaves, respectively, to the emitted leaves radiation reflected by the soil (also apply for leaf emission reflected by other leaves) [-]
e_a, e_0	Air vapor pressure at the reference and aerodynamic levels, respectively [Pa].
G, H, λE	Ground, sensible and latent heat fluxes [W m^{-2}]
h, d	Vegetation height and leaf width [m]
K_g, K_z	Fractions/contribution of sunlit and shaded visible soil [-]
K_c, K_t	Contribution of sunlit and shaded leaves to out-of-canopy radiation [-]
$K_T; fd$	Clearness index [-] and fraction of diffuse radiation [-], respectively
$L(\theta_v), L_a^{\downarrow}$	Out-of-canopy radiance in the viewing direction and incoming sky radiation [W m^{-2}]
LAI, ɑ, Ω	Leaf area index [m^2 m^{-2}], foliage projection factor [-] and clumping index [-]
M	Hemispherical average gap frequency [-]
r_a	Aerodynamic resistance between the aerodynamic level and the reference level [s m^{-1}]
r_{as}/r_{av}	Aerodynamic resistance between the soil/vegetation and the aerodynamic level [s m^{-1}]
r_{vv}	Surface resistance between the aerodynamic and the reference levels [s m^{-1}]
$RG_{dir}, RG_{diff}, RG, C_s$	Direct, diffuse, total/global (BOA) and terrestrial (TOA) solar radiations, respectively [W m^{-2}]
R_n	Total (overall) net radiation [W m^{-2}]
$R_{ng,s};\ R_{ng,h}$	Net radiation over the sunlit (s) and shaded (h) soil [W m^{-2}]
$R_{nv,s};\ R_{nv,h}$	Net radiation over the sunlit and shaded vegetation [W m^{-2}]

T_a, T_0, T_{xx}	Air, aerodynamic and component temperatures [K]

References

Agam, N., Kustas, W. P., Anderson, M. C., Norman, J. M., Colaizzi, P. D., Howell, T. A., … Wilson, T. B. (2010). Application of the priestley-taylor approach in a two-source surface energy balance model. *Journal of Hydrometeorology*, *11*(1), 185–198. https://doi.org/10.1175/2009JHM1124.1

Annear, R. L., & Wells, S. A. (2007). A comparison of five models for estimating clear-sky solar radiation. *Water Resources Research*, *43*(10). https://doi.org/10.1029/2006WR005055

Bian, Z., Cao, B., Li, H., Du, Y., Lagouarde, J. P., Xiao, Q., & Liu, Q. (2018). An analytical four-component directional brightness temperature model for crop and forest canopies. *Remote Sensing of Environment*, *209*(March), 731–746. https://doi.org/10.1016/j.rse.2018.03.010

Boulet, G., Mougenot, B., Lhomme, J. P., Fanise, P., Lili-Chabaane, Z., Olioso, A., … Lagouarde, J. P. (2015). The SPARSE model for the prediction of water stress and evapotranspiration components from thermal infra-red data and its evaluation over irrigated and rainfed wheat. *Hydrology and Earth System Sciences*, *19*(11), 4653–4672. https://doi.org/10.5194/hess-19-4653-2015

Boulet, G., Olioso, A., Ceschia, E., Marloie, O., Coudert, B., Rivalland, V., … Chehbouni, G. (2012). An empirical expression to relate aerodynamic and surface temperatures for use within single-source energy balance models. *Agricultural and Forest Meteorology*, *161*, 148–155. https://doi.org/10.1016/j.agrformet.2012.03.008

Boulet, Gilles, Delogu, E., Saadi, S., Chebbi, W., Olioso, A., Mougenot, B., … Lagouarde, J. P. (2018). Evapotranspiration and evaporation/transpiration partitioning with dual source energy balance models in agricultural lands. *Proceedings of the International Association of Hydrological Sciences*, *380*, 17–22. https://doi.org/10.5194/piahs-380-17-2018

Braud, I., Dantas-Antonino, A. C. C., Vauclin, M., Thony, J. L. L., & Ruelle, P. (1995). A simple soil-plant-atmosphere transfer model (SiSPAT) development and field verification. *Journal of Hydrology*, *166*(3–4), 213–250. https://doi.org/10.1016/0022-1694(94)05085-C

Brutsaert, W. (1975). On a derivable formula for long-wave radiation from clear skies. *Water Resources Research*, *11*(5), 742–744. https://doi.org/10.1029/WR011i005p00742

Brutsaert, W. (1982). *Evaporation into the Atmosphere*. https://doi.org/10.1007/978-94-017-1497-6

Campbell, G. S., & Norman, J. M. (1998). Radiation Fluxes in Natural Environments. In *An Introduction to Environmental Biophysics* (pp. 167–184). https://doi.org/10.1007/978-1-4612-1626-1_11

Cao, B., Guo, M., Fan, W., Xu, X., Peng, J., Ren, H., … Liu, Q. (2018). A new directional canopy emissivity model based on spectral invariants. *IEEE Transactions on Geoscience and Remote Sensing*, *56*(12), 6911–6926. https://doi.org/10.1109/TGRS.2018.2845678

Cao, B., Liu, Q., Du, Y., Roujean, J. L., Gastellu-Etchegorry, J. P., Trigo, I. F., … Xiao, Q. (2019). A review of earth surface thermal radiation directionality observing and modeling: Historical development, current status and perspectives. *Remote Sensing of Environment*, *232*(October 2018), 111304.

https://doi.org/10.1016/j.rse.2019.111304

Carrer, D., Roujean, J. L., Lafont, S., Calvet, J. C., Boone, A., Decharme, B., … Gastellu-Etchegorry, J. P. (2013). A canopy radiative transfer scheme with explicit FAPAR for the interactive vegetation model ISBA-A-gs: Impact on carbon fluxes. *Journal of Geophysical Research: Biogeosciences*, *118*(2), 888–903. https://doi.org/10.1002/jgrg.20070

Cellier, P., & Olioso, A. (1993). A simple system for automated long-term Bowen ratio measurement. *Agricultural and Forest Meteorology*, *66*(1–2), 81–92. https://doi.org/10.1016/0168-1923(93)90083-T

Chebbi, W., Boulet, G., Le Dantec, V., Lili Chabaane, Z., Fanise, P., Mougenot, B., & Ayari, H. (2018). Analysis of evapotranspiration components of a rainfed olive orchard during three contrasting years in a semi-arid climate. *Agricultural and Forest Meteorology*, *256–257*(January), 159–178. https://doi.org/10.1016/j.agrformet.2018.02.020

Chen, J. M., & Liu, J. (2020). Evolution of evapotranspiration models using thermal and shortwave remote sensing data. *Remote Sensing of Environment*, *237*(November 2019), 111594. https://doi.org/10.1016/j.rse.2019.111594

Colaizzi, P. D., Kustas, W. P., Anderson, M. C., Agam, N., Tolk, J. A., Evett, S. R., … O'Shaughnessy, S. A. (2012). Two-source energy balance model estimates of evapotranspiration using component and composite surface temperatures. *Advances in Water Resources*, *50*, 134–151. https://doi.org/10.1016/j.advwatres.2012.06.004

Collatz, G. J., Ball, J. T., Grivet, C., & Berry, J. A. (1991). Physiological and environmental regulation of stomatal conductance, photosynthesis and transpiration: a model that includes a laminar boundary layer. *Agricultural and Forest Meteorology*, *54*(2–4), 107–136. https://doi.org/10.1016/0168-1923(91)90002-8

Delogu, E., Boulet, G., Olioso, A., Garrigues, S., Brut, A., Tallec, T., … Lagouarde, J. P. (2018). Evaluation of the SPARSE dual-source model for predictingwater stress and evapotranspiration from thermal infrared data over multiple crops and climates. *Remote Sensing*, *10*(11). https://doi.org/10.3390/rs10111806

Delogu, E., Olioso, A., Alliès, A., Demarty, J., & Boulet, G. (2021). Evaluation of Multiple Methods for the Production of Continuous Evapotranspiration Estimates from TIR Remote Sensing. *Remote Sensing*, *13*(6), 1086. https://doi.org/10.3390/rs13061086

Duchemin, B., Hadria, R., Erraki, S., Boulet, G., Maisongrande, P., Chehbouni, A., … Simonneaux, V. (2006). Monitoring wheat phenology and irrigation in Central Morocco: On the use of relationships between evapotranspiration, crops coefficients, leaf area index and remotely-sensed vegetation indices. *Agricultural Water Management*, *79*(1), 1–27. https://doi.org/10.1016/j.agwat.2005.02.013

Duffour, C., Lagouarde, J. P., Olioso, A., Demarty, J., & Roujean, J. L. (2016). Driving factors of the directional variability of thermal infrared signal in temperate regions. *Remote Sensing of Environment*, *177*, 248–264. https://doi.org/10.1016/j.rse.2016.02.024

Duffour, C., Olioso, A., Demarty, J., Van der Tol, C., & Lagouarde, J. P. (2015). An evaluation of SCOPE: A tool to simulate the directional anisotropy of satellite-measured surface temperatures. *Remote Sensing of Environment*, *158*, 362–375. https://doi.org/10.1016/j.rse.2014.10.019

Er-Raki, S., Chehbouni, A., Ezzahar, J., Khabba, S., Boulet, G., Hanich, L., & Williams, D. (2009). Evapotranspiration partitioning from sap flow and eddy covariance techniques for olive orchards in semi-arid region. *Acta Horticulturae*, *846*, 201–208. https://doi.org/10.17660/ActaHortic.2009.846.21

Erbs, D. G., Klein, S. A., & Duffie, J. A. (1982). Estimation of the diffuse radiation fraction for hourly, daily and monthly-average global radiation. *Solar Energy*, *28*(4), 293–302. https://doi.org/10.1016/0038-092X(82)90302-4

François, C. (2002). The potential of directional radiometric temperatures for monitoring soil and leaf temperature and soil moisture status. *Remote Sensing of Environment*, *80*(1), 122–133. https://doi.org/10.1016/S0034-4257(01)00293-0

Francois, C., Ottle, C., & Prevot, L. (1997). Analytical parameterization of canopy directional emissivity and directional radiance in the thermal infrared. Application on the retrieval of soil and foliage temperatures using two directional measurements. *International Journal of Remote Sensing*, *18*(12), 2587–2621. https://doi.org/10.1080/014311697217495

Gentine, P., Entekhabi, D., Chehbouni, A., Boulet, G., & Duchemin, B. (2007). Analysis of evaporative fraction diurnal behaviour. *Agricultural and Forest Meteorology*, *143*(1–2), 13–29. https://doi.org/10.1016/j.agrformet.2006.11.002

Herrero, J., & Polo, M. J. (2012). Parameterization of atmospheric longwave emissivity in a mountainous site for all sky conditions. *Hydrology and Earth System Sciences*, *16*(9), 3139–3147. https://doi.org/10.5194/hess-16-3139-2012

Hoedjes, J. C. B., Chehbouni, A., Ezzahar, J., Escadafal, R., & De Bruin, H. A. R. (2007). Comparison of large aperture scintillometer and eddy covariance measurements: Can thermal infrared data be used to capture footprint-induced differences? *Journal of Hydrometeorology*, *8*(2), 144–159. https://doi.org/10.1175/JHM561.1

Huxman, T. E., Wilcox, B. P., Breshears, D. D., Scott, R. L., Snyder, K. A., Small, E. E., … Jackson, R. B. (2005). Ecohydrological implications of woody plant encroachment. *Ecology*, *86*(2), 308–319. https://doi.org/10.1890/03-0583

Idso, S. B. (1981). A set of equations for full spectrum and 8- to 14-µm and 10.5- to 12.5-µm thermal radiation from cloudless skies. *Water Resources Research*, *17*(2), 295–304. https://doi.org/10.1029/WR017i002p00295

Iqbal, M. (1983). *An Introduction to Solar Radiation*. New York: Academic Press.

Kimes, D. S., & Kirchner, J. A. (1983). Directional radiometric measurements of row-crop temperatures. *International Journal of Remote Sensing*, *4*(2), 299–311. https://doi.org/10.1080/01431168308948548

Kustas, W. P., & Norman, J. M. (1996). Use of remote sensing for evapotranspiration monitoring over land surfaces. *Hydrological Sciences Journal*, *41*(4), 495–516. https://doi.org/10.1080/02626669609491522

Lagouarde, J.-P., Bhattacharya, B. K., Crébassol, P., Gamet, P., Adlakha, D., Murthy, C. S., … Sarkar, S. S. (2019). Indo-French High-Resolution Thermal Infrared Space Mission for Earth Natural Resources Assessment and Monitoring – Concept and Definition of Trishna. *ISPRS - International Archives of the Photogrammetry, Remote Sensing and Spatial Information Sciences*, *XLII-3/W6*(February), 403–

407. https://doi.org/10.5194/isprs-archives-xlii-3-w6-403-2019

Lagouarde, J., & Bhattacharya, B. K. (2018). TRISHNA : a new high spatio-temporal resolution Indian-French mission in the thermal infrared. *Remote Sensing and Hydrology Symposium (ICRS-IAHS)*, 2024.

Lagouarde, J. P., Bach, M., Sobrino, J. A., Boulet, G., Briottet, X., Cherchali, S., … Fargant, G. (2013). The MISTIGRI thermal infrared project: Scientific objectives and mission specifications. *International Journal of Remote Sensing*, *34*(9–10), 3437–3466. https://doi.org/10.1080/01431161.2012.716921

Lagouarde, J. P., Dayau, S., Moreau, P., & Guyon, D. (2014). Directional anisotropy of brightness surface temperature over vineyards: Case study over the Medoc Region (SW France). *IEEE Geoscience and Remote Sensing Letters*, *11*(2), 574–578. https://doi.org/10.1109/LGRS.2013.2282492

Li, J., Fan, W., Liu, Y., Zhu, G., Peng, J., & Xu, X. (2017). Estimating savanna clumping index using hemispherical photographs integrated with high resolution remote sensing images. *Remote Sensing*, *9*(1). https://doi.org/10.3390/rs9010052

Medlyn, B. E., Duursma, R. A., Eamus, D., Ellsworth, D. S., Prentice, I. C., Barton, C. V. M., … Wingate, L. (2011). Reconciling the optimal and empirical approaches to modelling stomatal conductance. *Global Change Biology*, *17*(6), 2134–2144. https://doi.org/10.1111/j.1365-2486.2010.02375.x

Merlin, O., Al Bitar, A., Rivalland, V., Béziat, P., Ceschia, E., & Dedieu, G. (2011). An analytical model of evaporation efficiency for unsaturated soil surfaces with an arbitrary thickness. *Journal of Applied Meteorology and Climatology*, *50*(2), 457–471. https://doi.org/10.1175/2010JAMC2418.1

Nilson, T. (1971). A theoretical analysis of the frequency of gaps in plant stands. *Agricultural Meteorology*, *8*(1966), 25–38. https://doi.org/10.1016/0002-1571(71)90092-6

Noilhan, J., & Planton, S. (1989). A Simple Parameterization of Land Surface Processes for Meteorological Models. *Monthly Weather Review*, *117*(3), 536–549. https://doi.org/10.1175/1520-0493(1989)117<0536:ASPOLS>2.0.CO;2

Norman, J. M., Kustas, W. P., & Humes, K. S. (1995). Source approach for estimating soil and vegetation energy fluxes in observations of directional radiometric surface temperature. *Agricultural and Forest Meteorology*, *77*(3–4), 263–293. https://doi.org/10.1016/0168-1923(95)02265-Y

Olioso, A. (1995). Estimating the difference between brightness and surface temperatures for a vegetal canopy. *Agricultural and Forest Meteorology*, *72*(3–4), 237–242. https://doi.org/10.1016/0168-1923(94)02163-E

Olioso, A., Carlson, T. N., & Brisson, N. (1996). Simulation of diurnal transpiration and photosynthesis of a water stressed soybean crop. *Agricultural and Forest Meteorology*, *81*(1–2), 41–59. https://doi.org/10.1016/0168-1923(95)02297-X

Olioso, A., Taconet, O., Mehrez, B., Nivoit, D., Promayon, F., & Rahmoune, L. (1995). Estimation of evapotranspiration using SVAT models and surface IR temperature. *1995 International Geoscience and Remote Sensing Symposium, IGARSS '95. Quantitative Remote Sensing for Science and Applications*, *1*, 516–518. https://doi.org/10.1109/IGARSS.1995.520324

Santanello, J. A., & Friedl, M. A. (2003). Diurnal covariation in soil heat flux and net radiation. *Journal of Applied Meteorology*, *42*(6), 851–862. https://doi.org/10.1175/1520-0450(2003)042<0851:DCISHF>2.0.CO;2

945 Schlesinger, W. H., & Jasechko, S. (2014). Transpiration in the global water cycle. *Agricultural and Forest*
946 *Meteorology*, *189–190*, 115–117. https://doi.org/10.1016/j.agrformet.2014.01.011

947 Shuttleworth, W. J., & Gurney, R. J. (1990). The theoretical relationship between foliage temperature
948 and canopy resistance in sparse crops. *Quarterly Journal of the Royal Meteorological Society*,
949 *116*(492), 497–519. https://doi.org/10.1002/qj.49711649213

950 Sinclair, T. R., Murphy, C. E., & Knoerr, K. R. (1976). Development and Evaluation of Simplified Models
951 for Simulating Canopy Photosynthesis and Transpiration. *The Journal of Applied Ecology*, *13*(3),
952 813. https://doi.org/10.2307/2402257

953 Su, Z. (2002). The Surface Energy Balance System (SEBS) for estimation of turbulent heat fluxes.
954 *Hydrology and Earth System Sciences*, *6*(1), 85–100. https://doi.org/10.5194/hess-6-85-2002

955 Taconet, O., Bernard, R., & Vidal-Madjar, D. (1986). Evapotranspiration over an Agricultural Region Using
956 a Surface Flux/Temperature Model Based on NOAA-AVHRR Data. *Journal of Climate and Applied*
957 *Meteorology*, *25*(3), 284–307. https://doi.org/10.1175/1520-
958 0450(1986)025<0284:EOAARU>2.0.CO;2

959 Williams, D. G., Cable, W., Hultine, K., Hoedjes, J. C. B., Yepez, E. A., Simonneaux, V., … Timouk, F. (2004).
960 Evapotranspiration components determined by stable isotope, sap flow and eddy covariance
961 techniques. *Agricultural and Forest Meteorology*, *125*(3–4), 241–258.
962 https://doi.org/10.1016/j.agrformet.2004.04.008

963 Yan, B. Y., Xu, X. R., & Fan, W. J. (2012). A unified canopy bidirectional reflectance (BRDF) model for row
964 crops. *Science China Earth Sciences*, *55*(5), 824–836. https://doi.org/10.1007/s11430-012-4380-9

965